Hindawi
International Journal of Energy Research
Volume 2024, Article ID 2316636, 26 pages
https://doi.org/10.1155/2024/2316636

WILEY | Hindawi

Research Article

Coupled Insights into Structural, Electronic, and Optical Properties of $GeTMS_3$(TM=Sc, Fe, Zn) Sulfide Perovskite across Different Phases: Ab Initio Study

Anwar M. Bakeer, Nada T. Mahmoud, and Riad Shaltaf

Physics Department, The University of Jordan, 11942 Amman, Jordan

Correspondence should be addressed to Riad Shaltaf; r.shaltaf@ju.edu.jo

Received 7 November 2023; Revised 20 January 2024; Accepted 27 February 2024; Published 8 April 2024

Academic Editor: Chaofan Sun

The structural stability analysis of various phases of GeTMS3(TM=Sc, Fe, Zn) sulfide perovskite has been conducted utilizing the WIEN2k package. This investigation leverages density functional theory (DFT) within the full potential linearized augmented plane wave (FP-LAPW) method, employing GGA-mBJ potentials. The focus of this study has encompassed the computation of structural, magnetic, and optical attributes across distinct $GeTMS_3$ phases. These materials have been identified as promising contenders for applications in photovoltaics and spintronics. The study reveals the stability of various phases, with the orthorhombic phase proving energetically favorable for $GeScS_3$ and $GeZnS_3$, and the tetragonal phase for $GeFeS_3$. Magnetic analyses indicate favorable ferromagnetic behavior in $GeFeS_3$ and nonmagnetic characteristics in $GeScS_3$ and $GeZnS_3$. Furthermore, electronic examinations unveil semimetallic and semiconducting behaviors in $GeScS_3$ and $GeZnS_3$ in the tetragonal, respectively, with $GeFeS_3$ exhibiting a half-metallic nature in the orthorhombic phase. Optical properties illustrate their potential as light harvesters, displaying characteristics suitable for energy conversion applications. This study contributes to a deeper understanding of sulfide perovskite properties, offering insights into potential applications in diverse technological fields.

1. Introduction

Energy conversion applications represent highly captivating materials for researchers today. Oxide and fluoride perovskite structures constitute a vast family of compounds with the stoichiometry ABX_3. In chalcogenide perovskites, the components A and B represent cations, while X corresponds to a group 6A element [1]. Beginning with Goldschmidt's initial investigations in 1926 [2], numerous studies have been undertaken to delve into the structural, electronic, and magnetic properties of perovskites, aiming to understand how these properties influence their potential for industrial applications [3–5].

Synthesized thin films of sulfide perovskite hold significant promise as candidates for photoelectron chemical water splitting and tandem solar energy conversion due to their wide bandgap, extensive light absorption, and photoluminescence capabilities [6, 7]. In an experimental study, stable thin films of chalcogenide perovskite were successfully fabricated, demonstrating potential applicability in optoelectronic devices such as photodetectors, light-emitting diodes, and photovoltaics [8]. Understanding the physical and electronic properties of such systems is advantageous to comprehend their potential applications. Perovskites are widely recognized for their diverse applications across various scientific and technological fields, owing to their broad range of electrooptical, mechanical, semiconducting, and insulating behaviors [9, 10].

In recent breakthroughs, researchers have successfully synthesized perovskite sulfides of transition metal chalcogenides. These compounds exhibit energy bandgaps across the infrared to the visible spectrum, showcasing promising attributes such as high absorption coefficients, minimal effective masses, and notable luminescence efficiency. Both

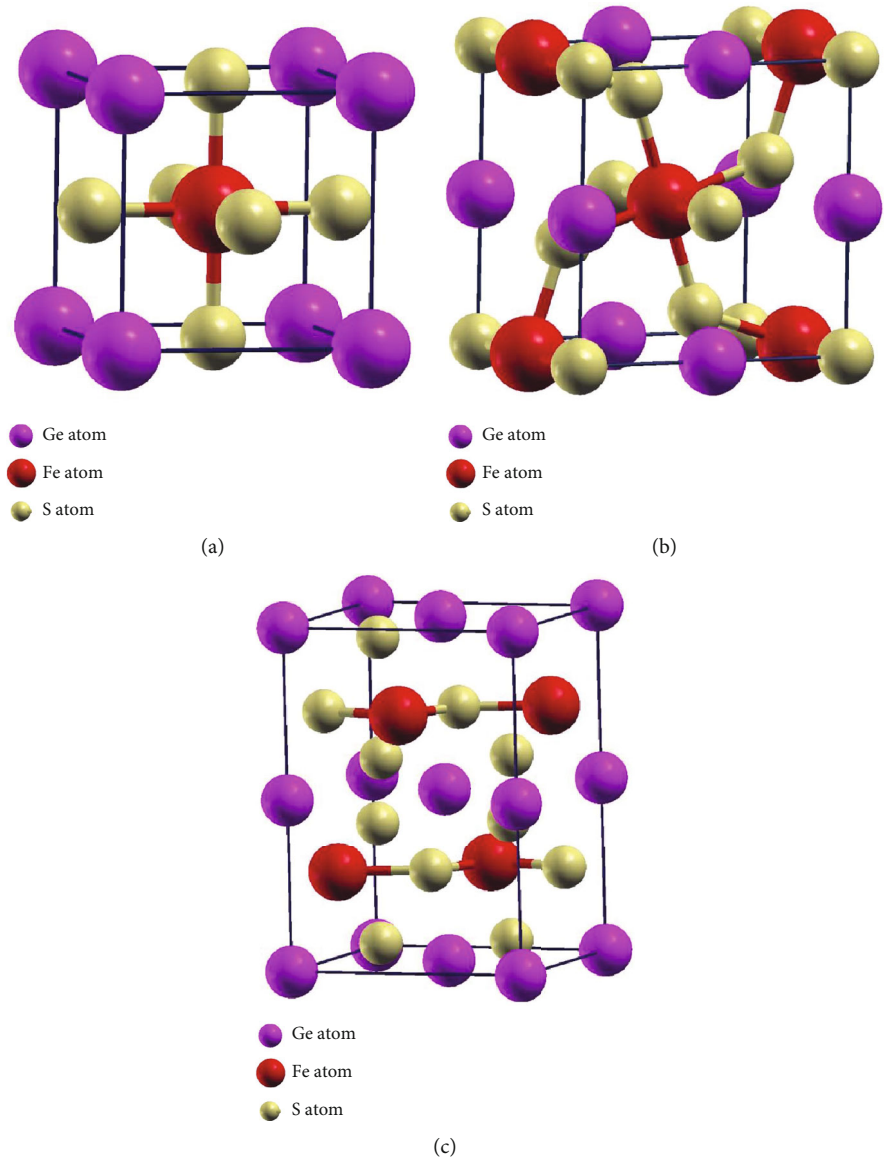

Figure 1: Unit cells of $GeTMS_3$ phases: (a) 221-Pm-3m, (b) 127-P4/mbm, and (c) 62-Pnma.

Table 1: Structure and optimized lattice constants for $GeTMS_3$ in different phases.

Structure	Phase space group	a (Å)	b (Å)	c (Å)	RMT Ge	RMT TM	RMT S
$GeScS_3$	221-Pm-3m	4.901	4.901	4.901	2.0	1.6	1.6
	127-P4/mbm	6.416	6.416	5.186	1.8	1.8	1.7
	62-Pnma	6.624	9.150	6.407	1.8	2.1	1.6
$GeFeS_3$	221-Pm-3m	4.536	4.536	4.536	1.8	2.0	1.7
	127-P4/mbm	6.109	6.109	4.608	1.8	1.8	1.7
	62-Pnma	6.528	9.222	6.230	1.8	2.1	1.6
$GeZnS_3$	221-Pm-3m	4.671	4.671	4.671	1.8	2.1	1.8
	127-P4/mbm	6.109	6.109	5.262	1.8	1.8	1.8
	62-Pnma	6.624	9.220	6.252	1.9	2.1	1.7

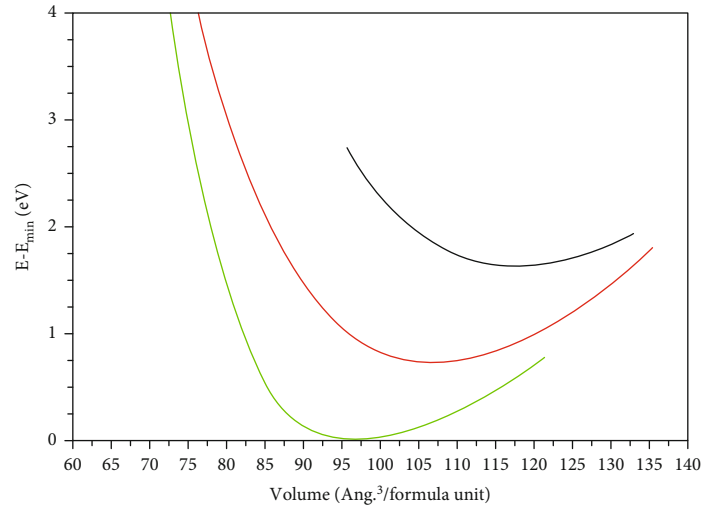

(a)

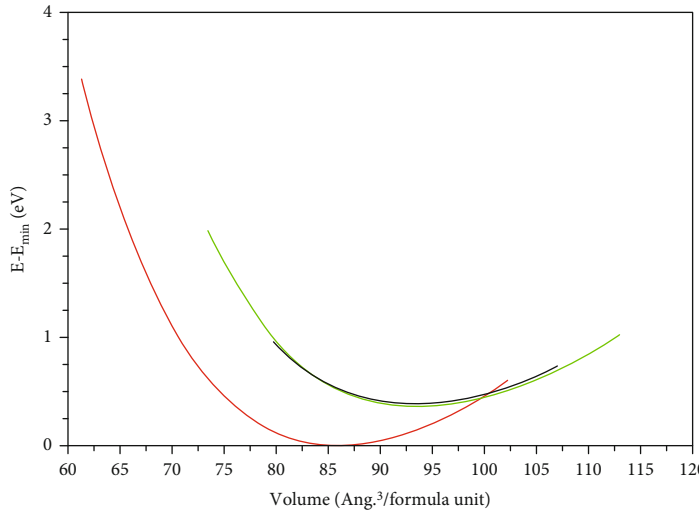

(b)

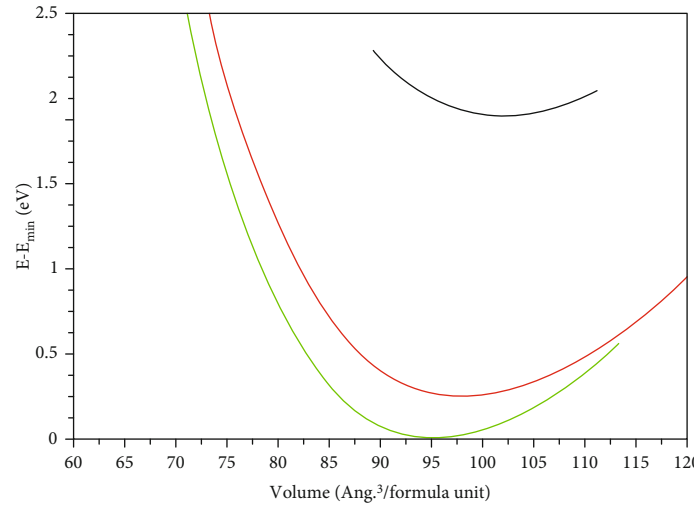

(c)

Figure 2: Volume optimization for $GeTMS_3$: (a) $GeScS_3$, (b) $GeFeS_3$, and (c) $GeZnS_3$. Black: 221-Pm-3m; red: 127-P4/mbm; green: 62-Pnma.

Table 2: Formation energy (Ry/atom) of $GeTMS_3$ in different space groups and magnetic phases.

Phase	Magnetic phase	E_{For} (Ry/atom)		
		$GeScS_3$	$GeFeS_3$	$GeZnS_3$
221-Pm-3m	FM	-4.125642	-2.654974	0.383643371
	AFM	-4.129842	-0.790936	0.392199707
	NM	-4.925742	-0.794163	0.12258207
	Magnetic stable phase	NM	FM	NM
127-P4/mbm	FM	-4.936249	-2.657930	0.106964112
	AFM	-2.288956	-0.704256	0.370307583
	NM	-2.288955	-0.707653	-0.301571869
	Magnetic stable phase	FM	FM	NM
62-Pnma	FM	-1.938481	-2.646873	0.113675
	AFM	-0.878480	-0.644178	4.76367537
	NM	-4.951581	-0.663400	-0.350513
	Magnetic stable phase	NM	FM	NM

Table 3: Total energy (Ry/unit cell) and formation energy for (Ry/atom) of ferromagnetic $GeFeS_3$ compound using mBJ and mBJ + U.

Phase	E_{total} (Ry/unit cell)		E_{For} (Ry/atom)	
	mBJ	mBJ ± U	mBJ	mBJ ± U
221-Pm-3m	-9121.147677	-9121.123864	-2.654974207	-2.6502116
127-P4/mbm	-18242.3249	-18242.2846	-2.65793023	-2.65390277
62-Pnma	-36484.4287	-36484.4146	-2.64687303	-2.64616861

Table 4: Magnetic moments (μB/formula unit) of $GeTMS_3$ in different phases.

Structure	Phase	TM	Ge	S	Interstitial	M_t (μ_B/F.U)	M_t (μ_B/F.U) using mBJ + U
$GeScS_3$	221-Pm-3m			NM			—
	127-P4/mbm	-0.06216	0.00004	0.00038 0.17056	-0.88881	1.694	—
	62-Pnma			NM			—
$GeFeS_3$	221-Pm-3m	2.80437	0.02407	0.25796	0.51649	4.071	4.059
	127-P4/mbm	3.10764	0.02080	0.11812 0.04393	0.53229	3.601	3.51
	62-Pnma	3.52372	0.00493	0.07068 0.07312	1.25095	4.001	4.007
$GeZnS_3$	NM						—

experimental and theoretical studies underscore their potential applicability in electronic, optical, and energy conversion technologies. Moreover, compounds like $AZrS_3$ (A=Ba, Sr), $LaYS_3$, and $Ba_3Zr_2S_7$ have experimentally revealed their direct bandgap nature, featuring bandgap energies ranging from 1.3 eV to 2.0 eV. These materials not only boast high absorption coefficients but also exhibit small effective masses and elevated luminescence efficiency, as demonstrated in recent investigations [11–16].

In a recent computational study focusing on chalcogenides perovskite, the investigation into the structural, optoelectronic, and thermodynamic properties of the $SnZrCH_3$ (CH=S, Se) compounds indicates that these materials exhibit an indirect bandgap nature. The bandgap energies are measured at 1.054 eV and 0.531 eV for $SnZrS_3$ and $SnZrSe_3$, respectively, at the mBJ-GGA level. Furthermore, calculations of optical absorption parameters highlight their possession of the highest absorption

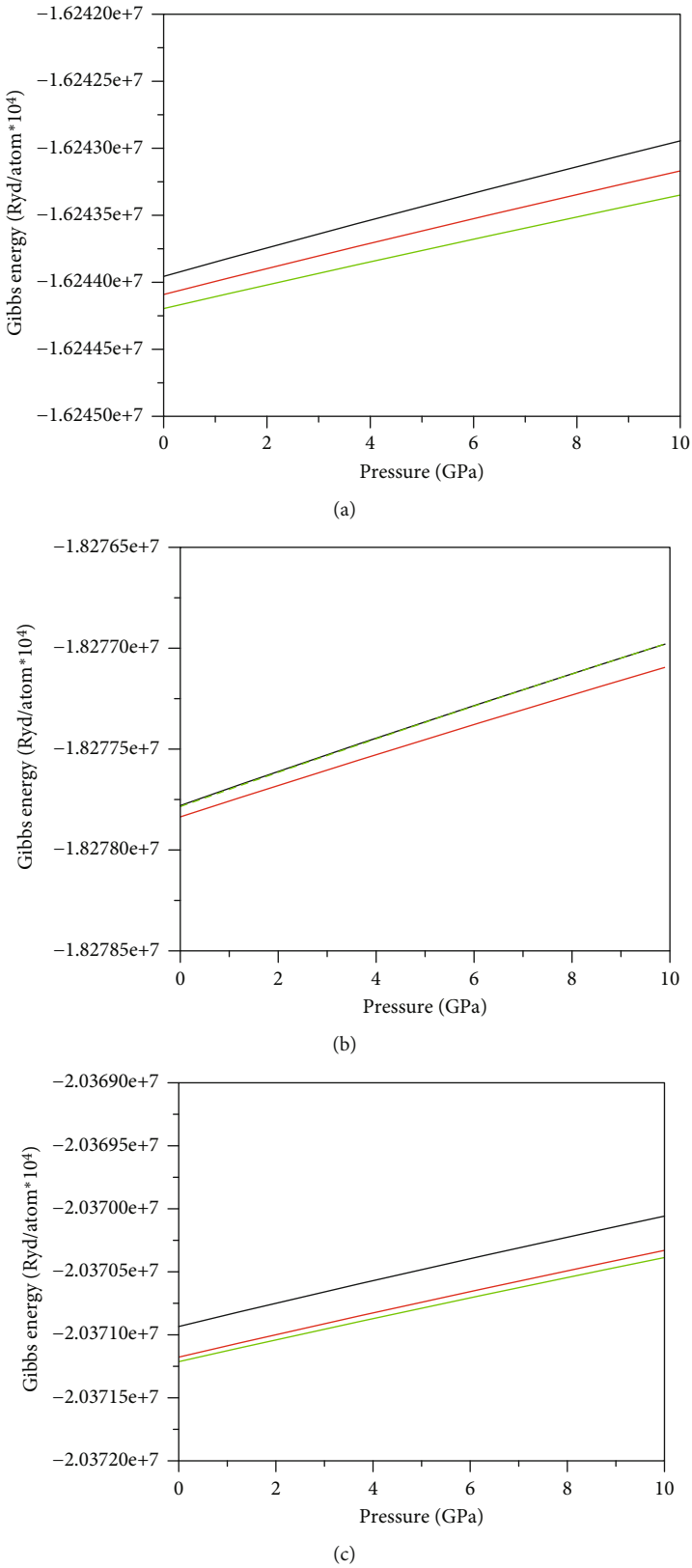

Figure 3: Gibbs free energy vs. pressure for $GeTMS_3$: (a) $GeScS_3$, (b) $GeFeS_3$, and (c) $GeZnS_3$. Black: 221-Pm-3m; red: 127-P4/mbm; green: 62-Pnma.

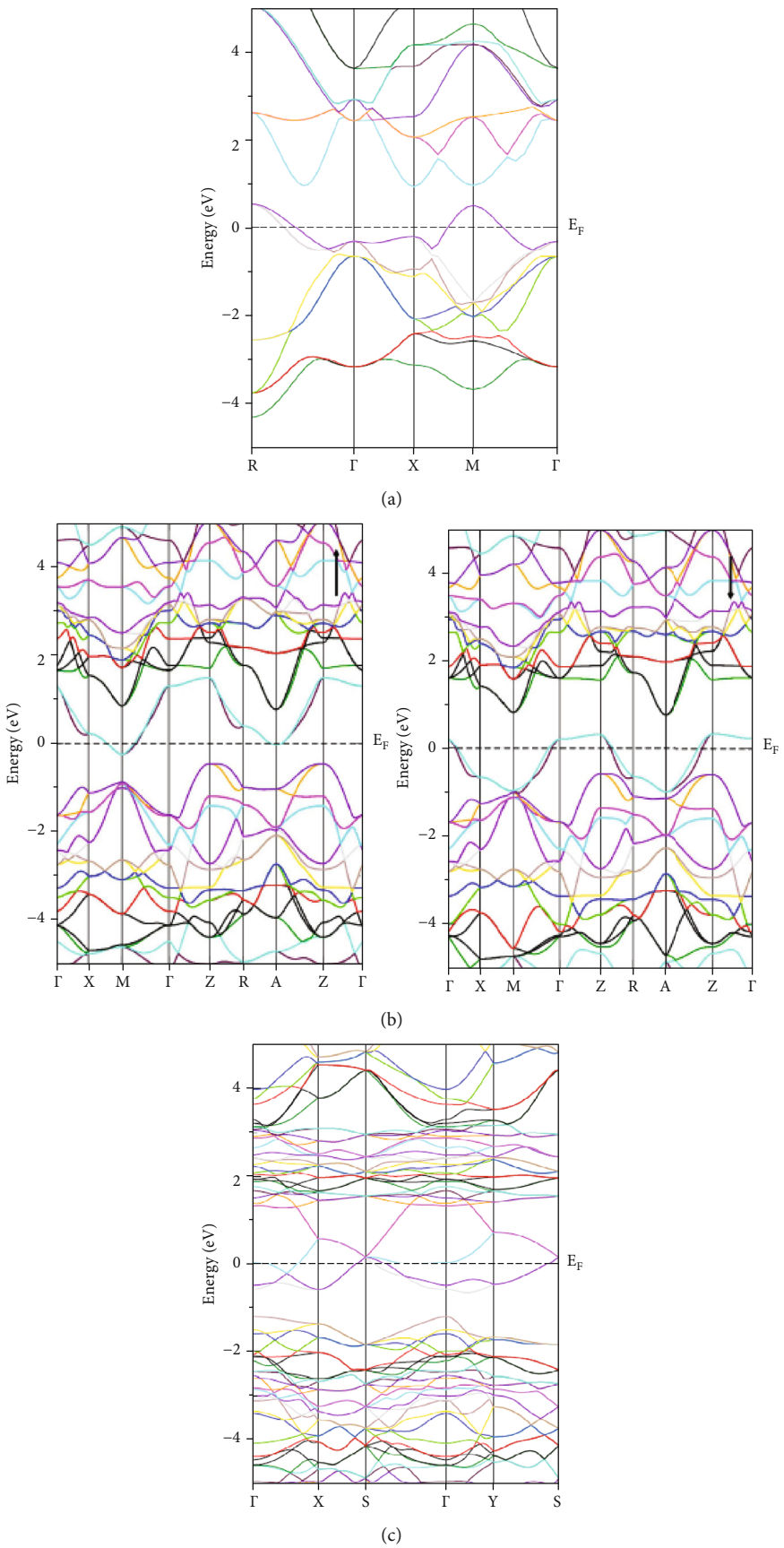

Figure 4: Electronic band structure for $GeScS_3$: (a) 221-Pm-3m, (b) 127-P4/mbm (spin up and spin down), and (c) 62-Pnma.

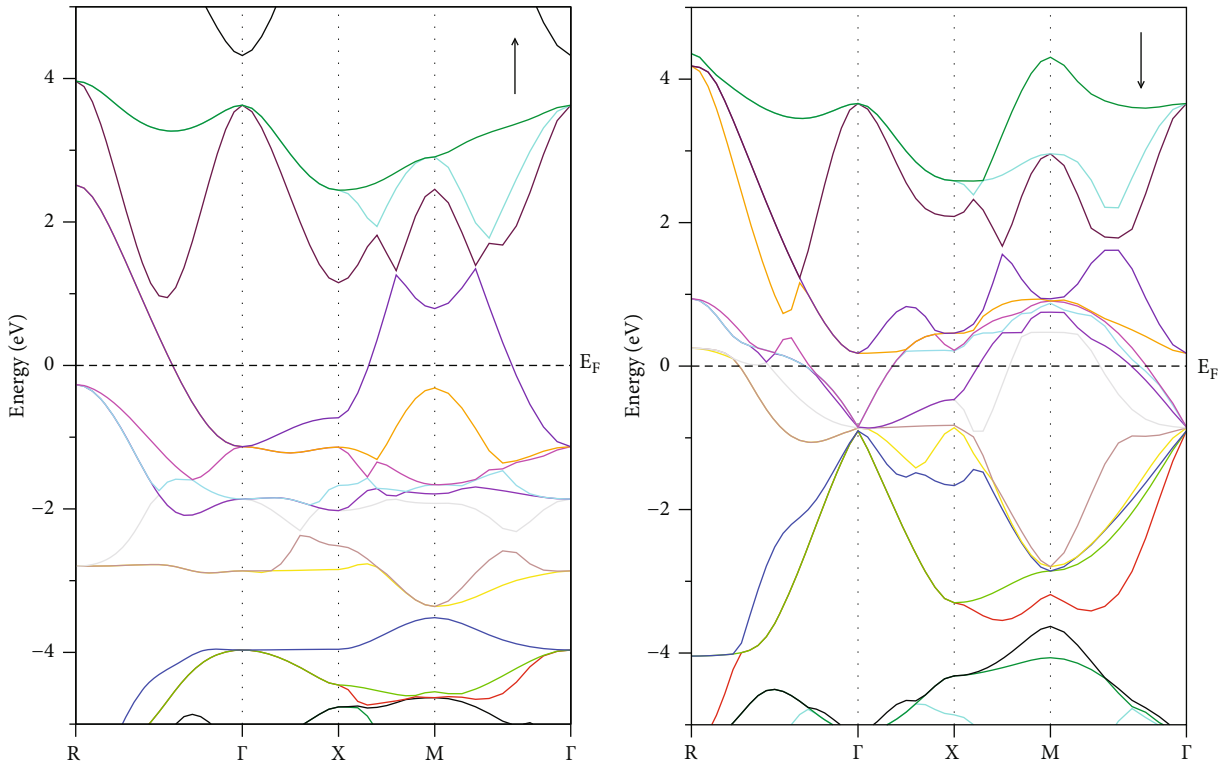

(a)

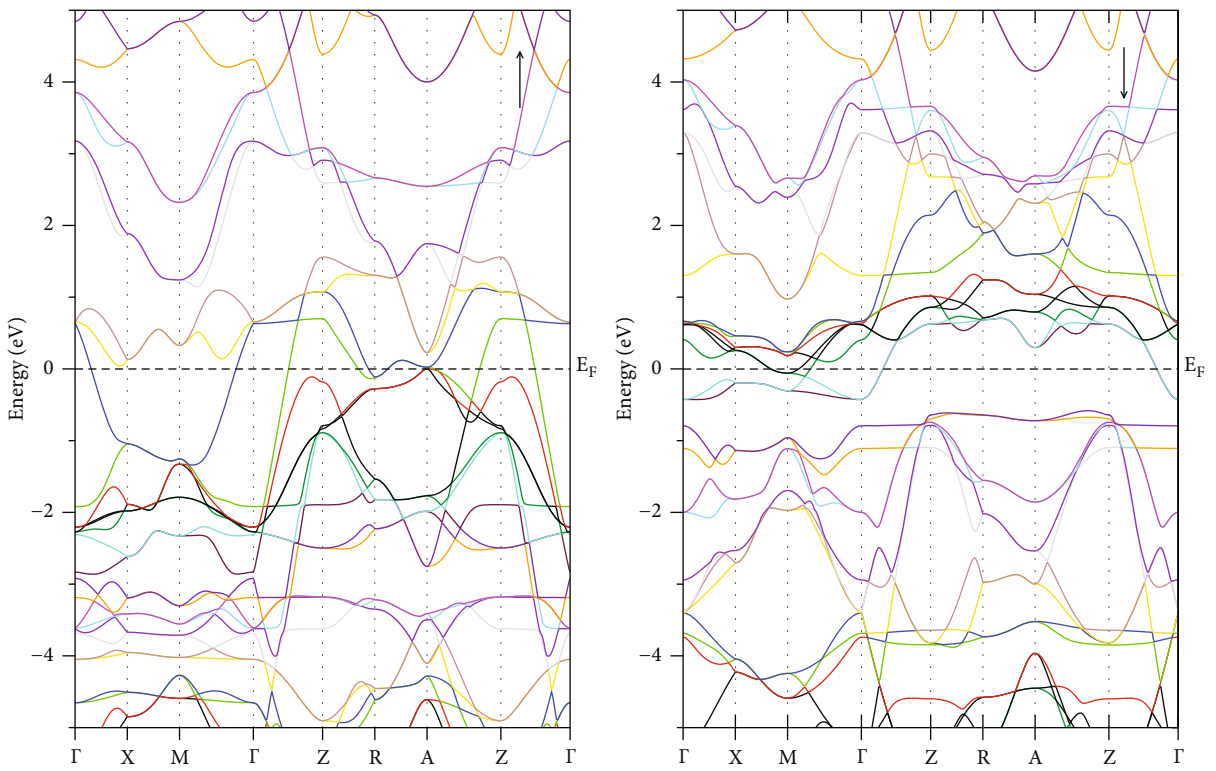

(b)

Figure 5: Continued.

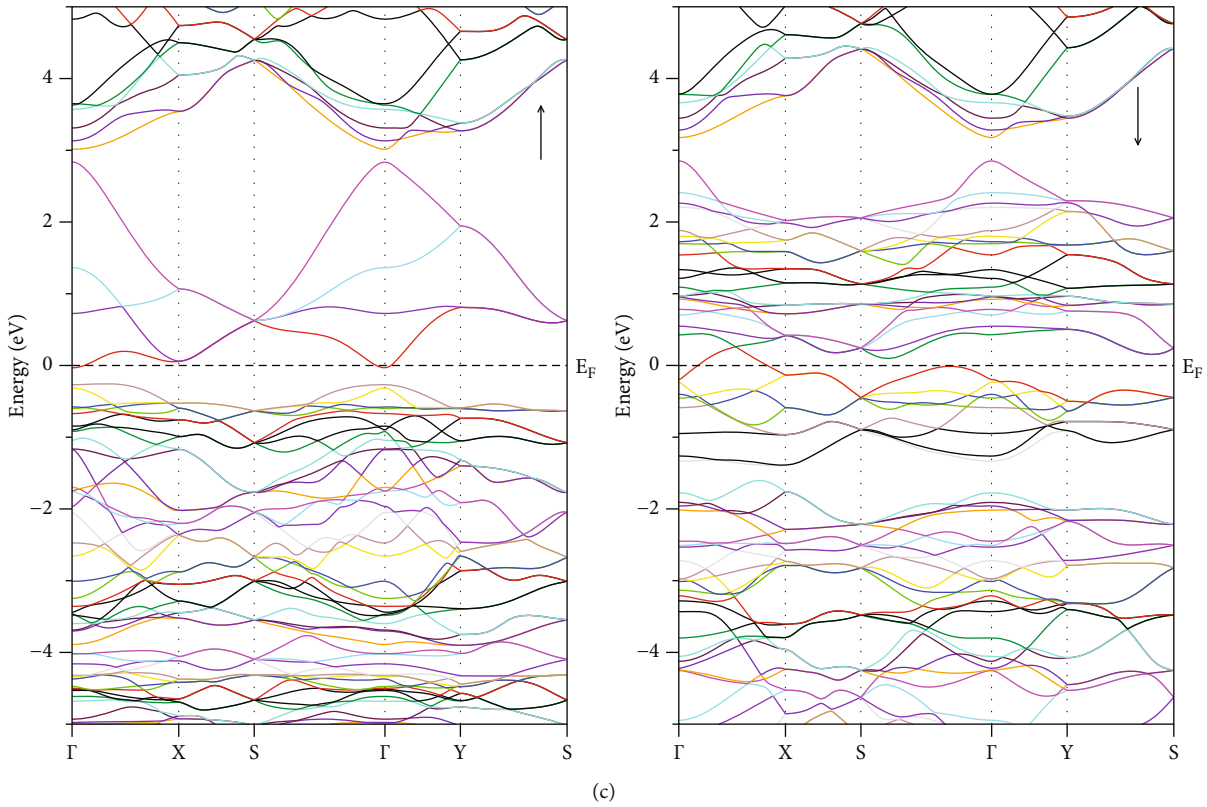

(c)

FIGURE 5: Electronic band structure for $GeFeS_3$: (a) 221-Pm-3m (spin up and spin down), (b) 127-P4/mbm (spin up and spin down), and (c) 62-Pnma (spin up and spin down).

coefficients in the ultraviolet (UV) region. Hence, the findings suggest that both $SnZrS_3$ and $SnZrSe_3$ compounds hold promise as potential candidates for photovoltaic applications [17].

Recently, we have undertaken a comprehensive exploration of various perovskite types. In a theoretical analysis of $TMScO_3$ (TM = 3d transition metal), we delved into the influence of 3d orbital filling on the bandgap. Significantly, our findings revealed a maximum bandgap of 5.496 eV for $CrScO_3$ [18]. Furthermore, we conducted a theoretical investigation into the impact of doping rare earth Eu ions into $Sr_{1-x}Eu_xLiF_3$ and $Ca_{1-x}Eu_xLiF_3$ fluoroperovskite systems. Intriguingly, all doped compounds exhibited 100% spin polarization at the Fermi level, displaying a spin half-metallic behavior with potential application in spintronics [19, 20].

In this paper, we focus on a comprehensive analysis of the structural, electronic, magnetic, and optical properties of $GeTMS_3$ sulfide perovskite across different phases. This investigation aims to contribute valuable insights into the intricate nature of these materials, providing a basis for their utilization in diverse technological fields.

2. Calculation Method

We employed the density functional theory (DFT)—full potential linearized augmented plane wave (FP-LAPW) method for our calculations [21], which was implemented using the WIEN2k package [22]. In our approach, we utilized both the generalized gradient approximation (GGA) [23] and the modified Becke-Johnson (mBJ) potential [24]. The chosen cutoff energy parameters were set to 16 Ryd for the plane waves in the interstitial region and 169 Ryd for the muffin-tin potential itself. This corresponds to a wave function expansion up to lmax = 10 within the muffin tins and up to lmax = 4 outside them. Furthermore, the charge density was Fourier-expanded to Gmax = 12. The core energy cutoff was set at −6.0 Ryd.

For *k*-point sampling within the irreducible Brillouin zone (IBZ), we employed a Monkhorst-pack grid of $14 \times 14 \times 14$ points for the cubic structure, with an equivalent number of points for the tetragonal and orthorhombic structures. Notably, a densely populated *k*-mesh of 8000 points was utilized for calculating optical properties. All structures underwent complete relaxation until the atomic forces were less than 1 mRy/bohr.

A charge convergence test was carried out with a tolerance of 0.0001 electron charge. The lattice constant was determined by optimizing the structure using the Murnaghan equation of state [25]. To calculate the density of states (DOS), we utilized the tetrahedron method with Blöchl corrections [26].

3. Results and Discussion

3.1. Structural, Electronic, and Magnetic Properties. The perovskite structure can manifest in various crystallographic

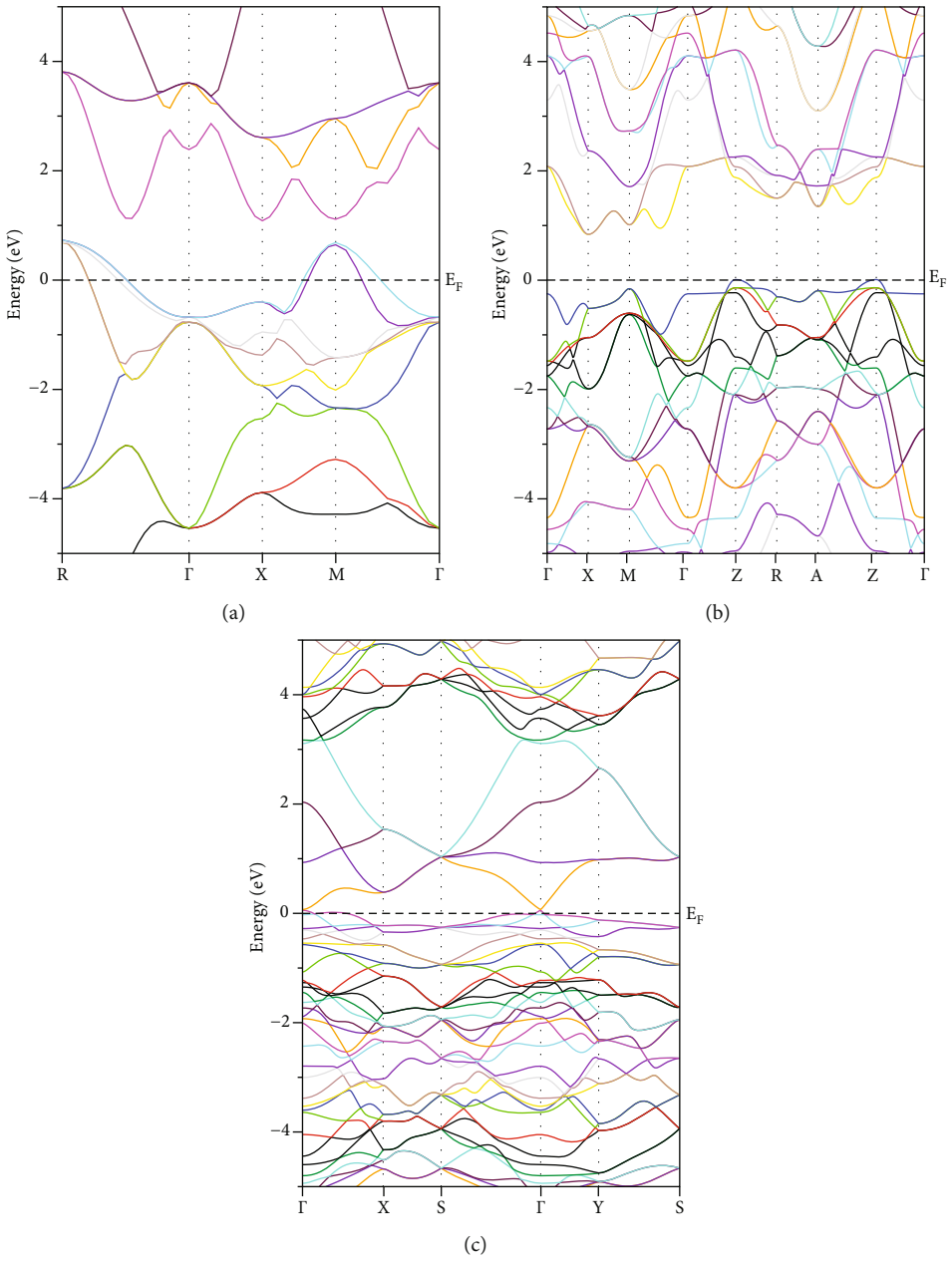

Figure 6: Electronic band structure for $GeZnS_3$: (a) 221-Pm-3m, (b) 127-P4/mbm, and (c) 62-Pnma.

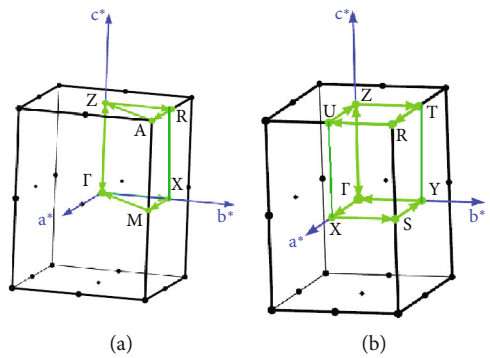

Figure 7: Crystal symmetry path points for (a) 127-P4/mbm and (b) 62-Pnma.

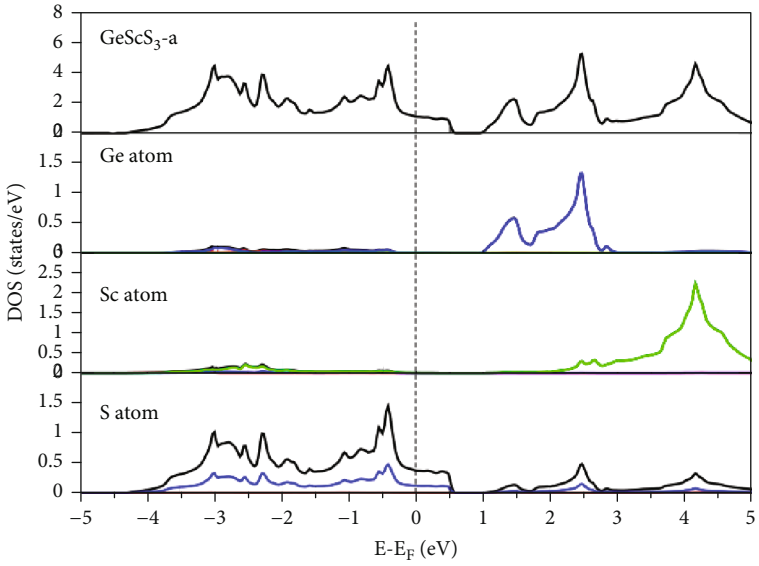

(a)

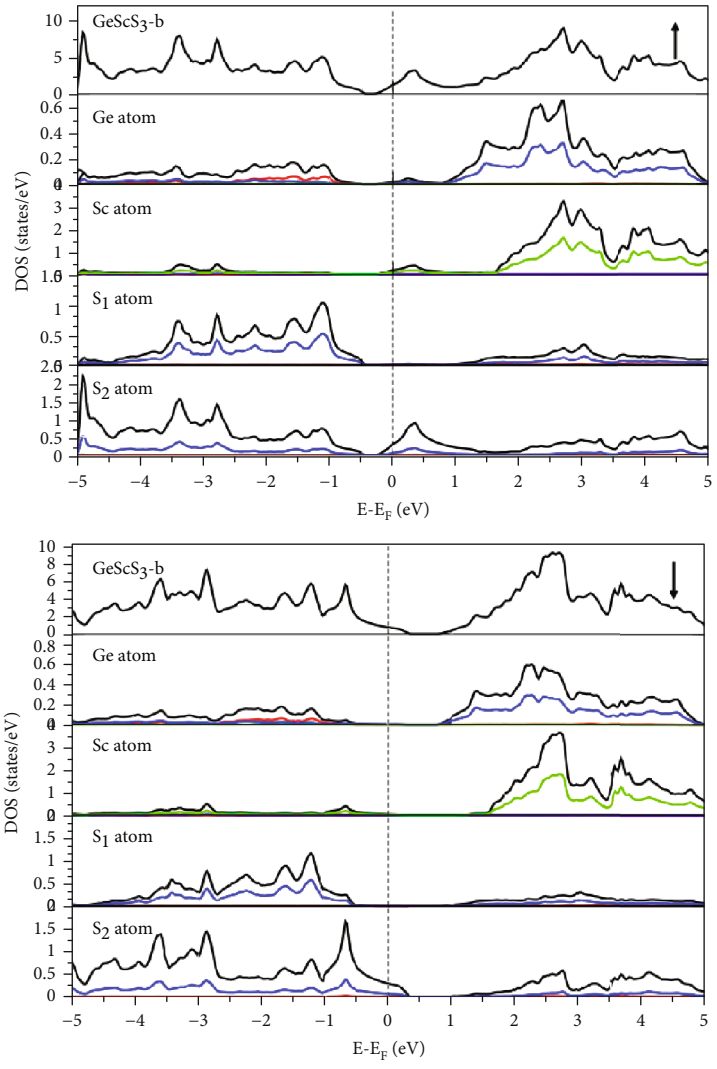

(b)

Figure 8: Continued.

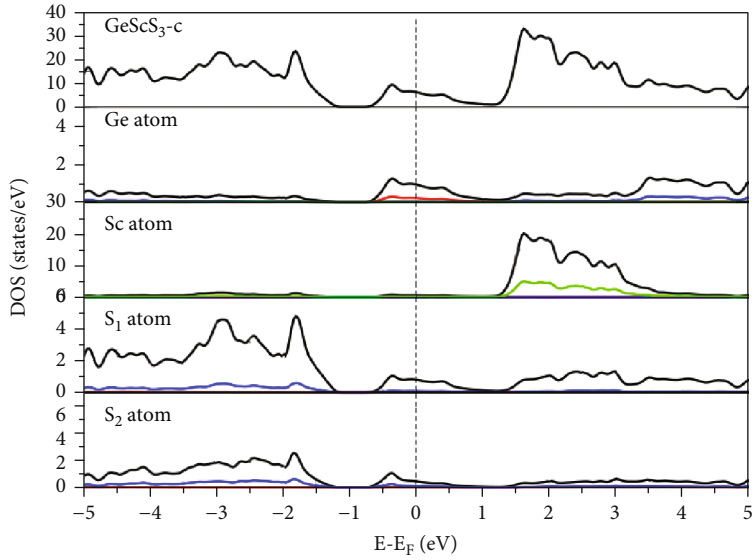

(c)

FIGURE 8: Total and partial density of states (TDOS and PDOS) for $GeScS_3$: (a) 221-Pm-3m, (b) 127-P4/mbm, and (c) 62-Pnma (black: TDOS; red: s-states; blue: p-states; green: d-states).

arrangements [2]. In this investigation, we focus on the three space groups, cubic (221-Pm-3m), tetragonal (127-P4/mbm), and orthorhombic (62-Pnma), as illustrated in Figure 1. For the cubic phase, we performed volume optimization, while for the tetragonal phase, optimization was conducted for both volume and c/a ratio, interchanging parameters to achieve the most stable configuration. Similarly, in the case of the orthorhombic phase, we optimized volume, c/a ratio, and b/a ratio by sequentially fixing two parameters in each trial and determining the third, as outlined in Table 1. In Figure 2, we present the calculated energy plotted against the volume per formula unit, fitted to the Murnaghan equation of state. The energetically favorable phases, which exhibit the lowest energy, are the orthorhombic phase for $GeScS_3$ and $GeZnS_3$, and the tetragonal phase for $GeFeS_3$.

Due to the absence of available experimental data, we assume an equal likelihood for each phase to occur naturally, pending experimental evidence to validate our predictive findings.

The stability of these compounds is intricately tied to the computation of formation energy. This metric is calculated as the difference between the total energy of the crystal and the combined energy of the crystal's individual components, as defined in the following equation [27]:

$$E_{\text{For}} = \frac{E_{\text{bulk}}^{\text{GeTMS}_3} - \left(xE^{\text{Ge}} + \text{y}E^{\text{TM}} + zE^{\text{S}}\right)}{x + y + z}, \quad (1)$$

In this context, $x(y, z)$ represents the count of Ge (TM, S) atoms within the unit cell. E^{Ge}, E^{TM}, and E^{S} represent the chemical potential for Ge, TM, and S atoms, respectively, within the stable bulk phase. Furthermore, $E_{\text{bulk}}^{\text{GeTMS}_3}$ signifies the total energy of $GeTMS_3$ within the unit cell.

Our analysis of the studied compounds considers each structural space group in three magnetic phases: ferromagnetic (FM), antiferromagnetic (AFM), and nonmagnetic (NM) phases. Table 2 illustrates the E_{For} values for each structure. It is evident that the most stable structure (highlighted in yellow) and the corresponding (nonmagnetic) 62-Pnma for both $GeScS_3$ and $GeZnS_3$ and the magnetic phase occur at (FM) 127-P4/mbm for $GeFeS_3$.

We have reevaluated our $GeFeS_3$ calculations by consistently applying Hubbard's correction through the mBJ + U approach across all space groups for the most favorable magnetic phases. The effective potential, sourced from literature and set at 2.2 eV [28], has been implemented at the iron (Fe) atom site. Despite the use of mBJ + U, the overall conclusion regarding this compound remains unchanged. The marginal variations observed in the total energy and formation energy of the compound are minimal, essentially rounding to zero. Additionally, all other deductions related to the band structure and density of states remain consistent (refer to Tables 3 and 4).

Another pivotal metric for evaluating the stability of different phases is the computation of Gibbs free energy against pressure (GPs). The correlation between Gibbs free energy and pressure is articulated as follows [29]:

$$dG = S\,dT + V\,dP + \mu\,dN. \quad (2)$$

In circumstances of exceedingly low temperature (absolute zero) and fixed N, as is the case here, $dG/dP = V$. From

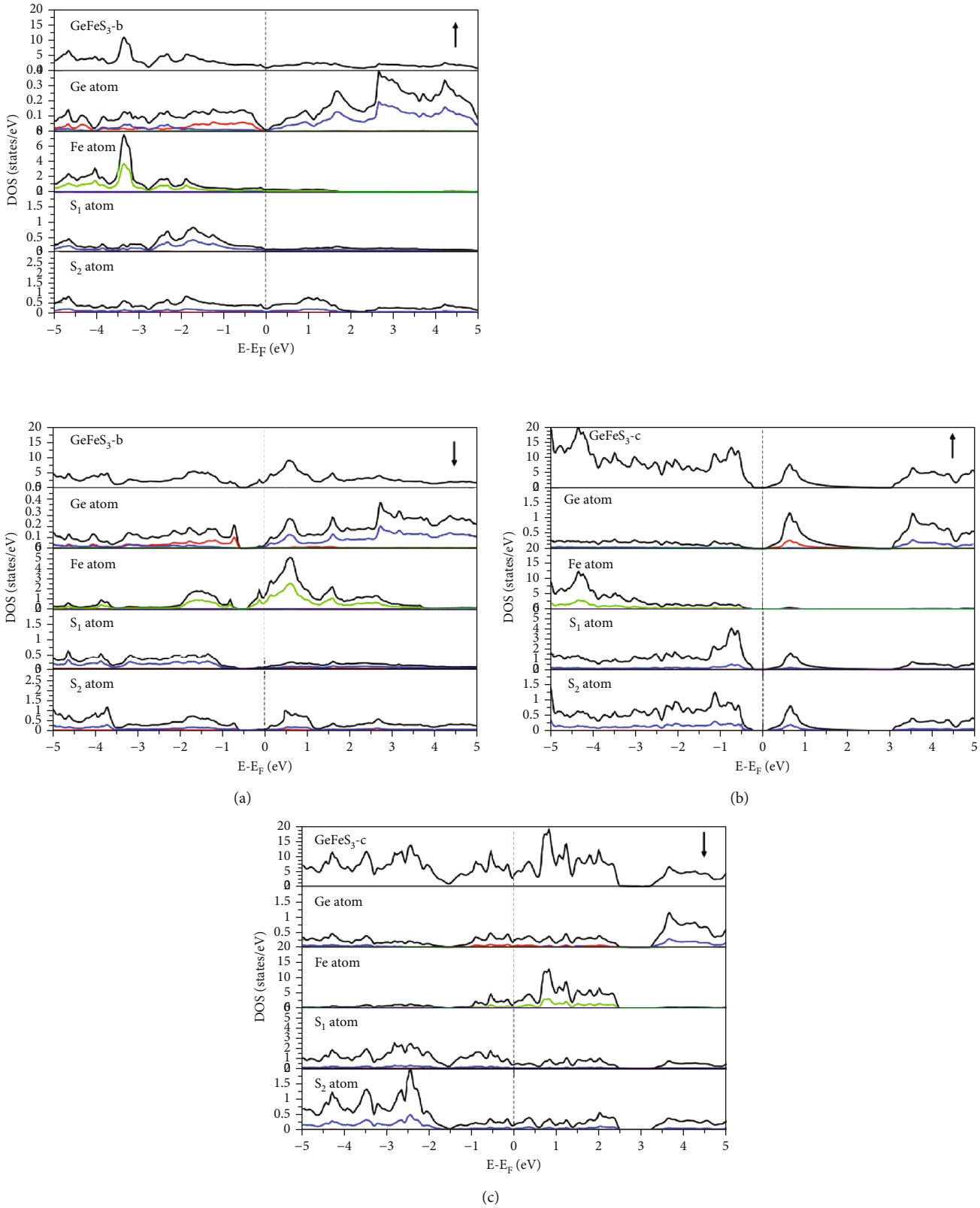

FIGURE 9: Total and partial density of states (TDOS and PDOS) for $GeFeS_3$: (a) 221-Pm-3m (spin up and spin down), (b) 127-P4/mbm (spin up and spin down), and (c) 62-Pnma (spin up and spin down) (black: TDOS; red: s-states; blue: p-states; green: d-states).

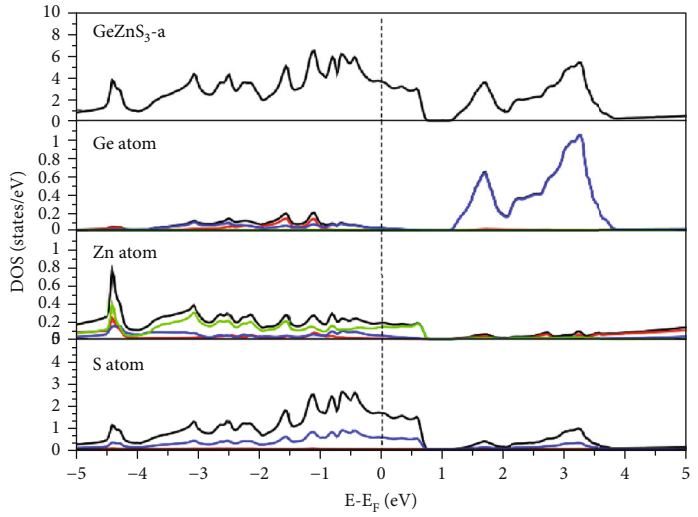

(a)

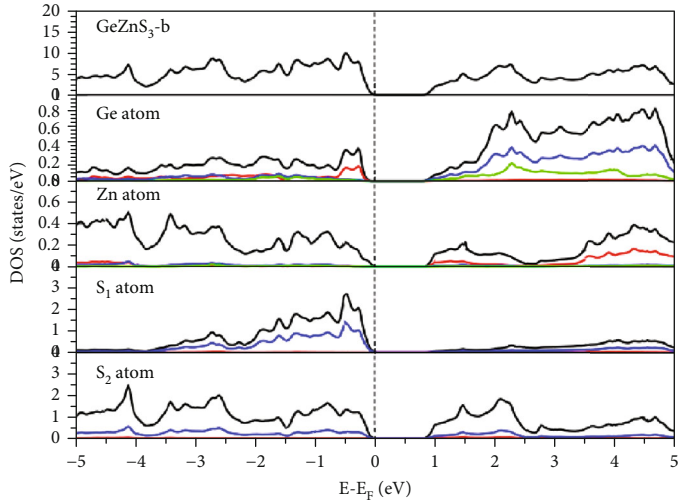

(b)

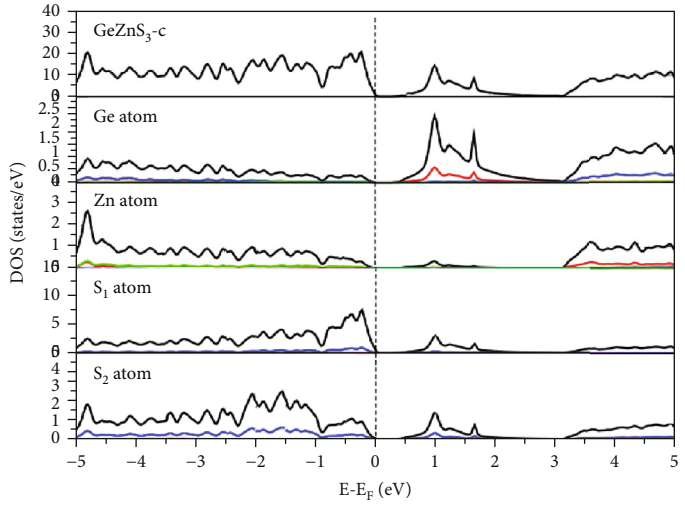

(c)

FIGURE 10: Total and partial density of states (TDOS and PDOS) for $GeZnS_3$: (a) 221-Pm-3m, (b) 127-P4/mbm, and (c) 62-Pnma (black: TDOS; red: s-states; blue: p-states; green: d-states).

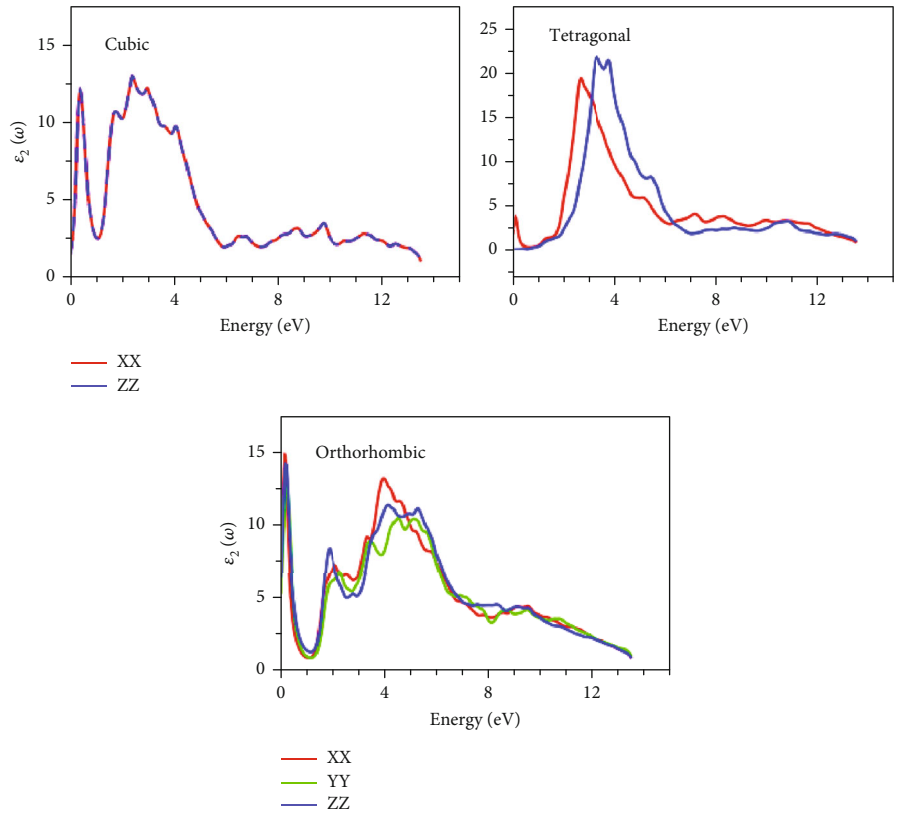

(a)

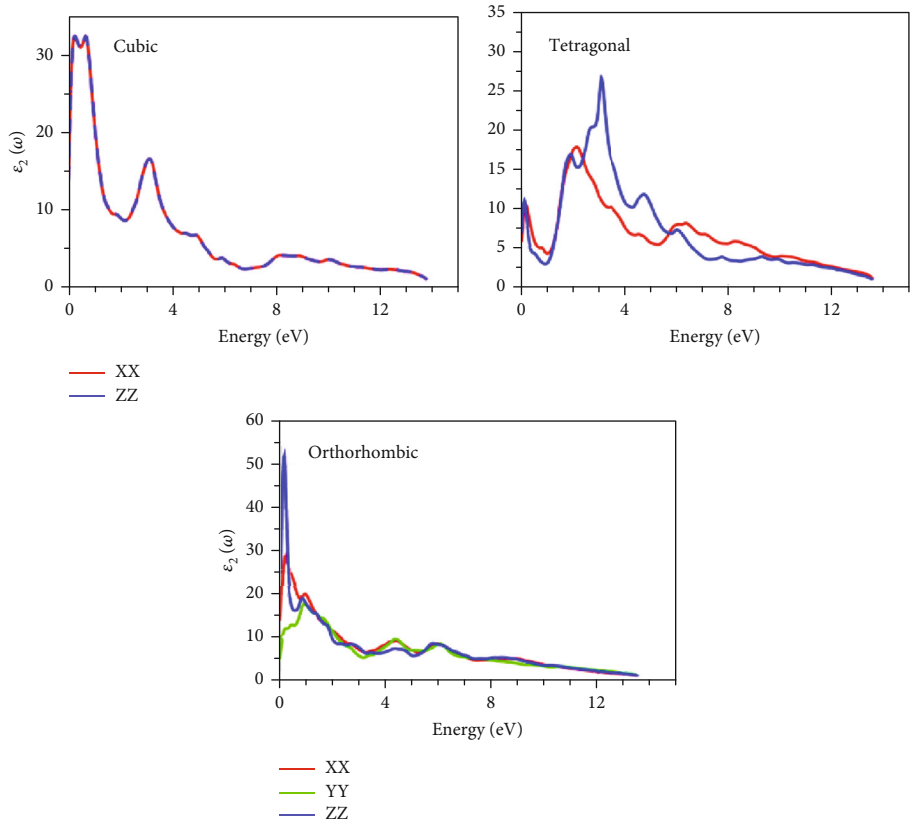

(b)

Figure 11: Continued.

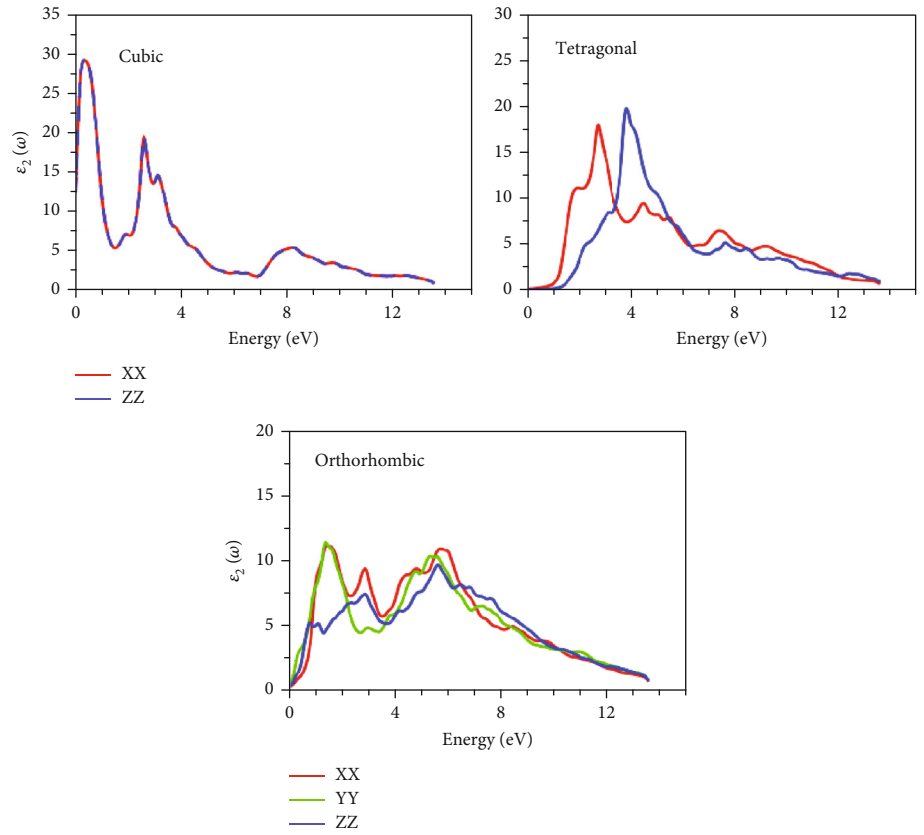

(c)

Figure 11: Imaginary part of dielectric function $\varepsilon_2(\omega)$ spectra of (a) $GeScS_3$, (b) $GeFeS_3$, and (c) $GeZnS_3$.

Table 5: Static optical properties for $GeScS_3$: dielectric constants $\varepsilon_1(0)$ and $\varepsilon_2(0)$, static refractive index $n(0)$, and static reflectivity $R(0)$ for all directions.

Phase	Direction	$\varepsilon_1(0)$	$\varepsilon_2(0)$	$n(0)$	$R(0)$
221-Pm-3m	*xx*	21.2	7.70	12.5	0.42
127-P4/mbm	*xx*	15.0	1.90	3.90	0.35
	zz	11.0	0.20	3.30	0.29
62-Pnma	*xx*	26.9	6.80	5.20	0.47
	yy	24.8	5.30	5.0	0.45
	zz	27.40	6.40	5.3	0.47

Table 6: Static optical properties for $GeFeS_3$: dielectric constants $\varepsilon_1(0)$ and $\varepsilon_2(0)$, static refractive index $n(0)$, and static reflectivity $R(0)$ for all directions.

Phase	Direction	$\varepsilon_1(0)$	$\varepsilon_2(0)$	$n(0)$	$R(0)$
221-Pm-3m	*xx*	65.60	13.6	8.10	0.61
127-P4/mbm	*xx*	30.10	5.80	5.50	0.48
	zz	31.20	6.90	5.60	0.49
62-Pnma	*xx*	60.50	13.9	7.80	0.60
	yy	36.0	5.50	6.10	0.51
	zz	79.50	26.10	9.10	0.65

Table 7: Static optical properties for $GeZnS_3$: dielectric constants $\varepsilon_1(0)$ and $\varepsilon_2(0)$, static refractive index $n(0)$, and static reflectivity $R(0)$ for all directions.

Phase	Direction	$\varepsilon_1(0)$	$\varepsilon_2(0)$	$n(0)$	$R(0)$
221-Pm-3m	*xx*	54.80	1.70	7.50	0.59
127-P4/mbm	*xx*	46.80	0.20	3.70	0.33
	zz	43.30	0.10	3.20	0.27
62-Pnma	*xx*	15.80	0.40	4.00	0.36
	yy	17.00	0.70	4.10	0.37
	zz	13.80	0.50	3.70	0.33

Figures 3(a) and 3(c), it becomes evident that the orthorhombic phase is the most stable for $GeScS_3$ ($GeZnS_3$). Conversely, for $GeFeS_3$, the tetragonal phase exhibits the highest stability (Figure 3(b)). This assertion is derived from the fact that these phases correspond to the shallowest lines. Notably, the calculations of Gibbs free energy align seamlessly with the Murnaghan equation of state, in regard to the stability of the structure.

The spin magnetic moments have been documented in Table 4. The magnetic behavior of the material is predominantly governed by the presence of the 3d-TM atom in site B, and this behavior is intricately tied to factors such as the

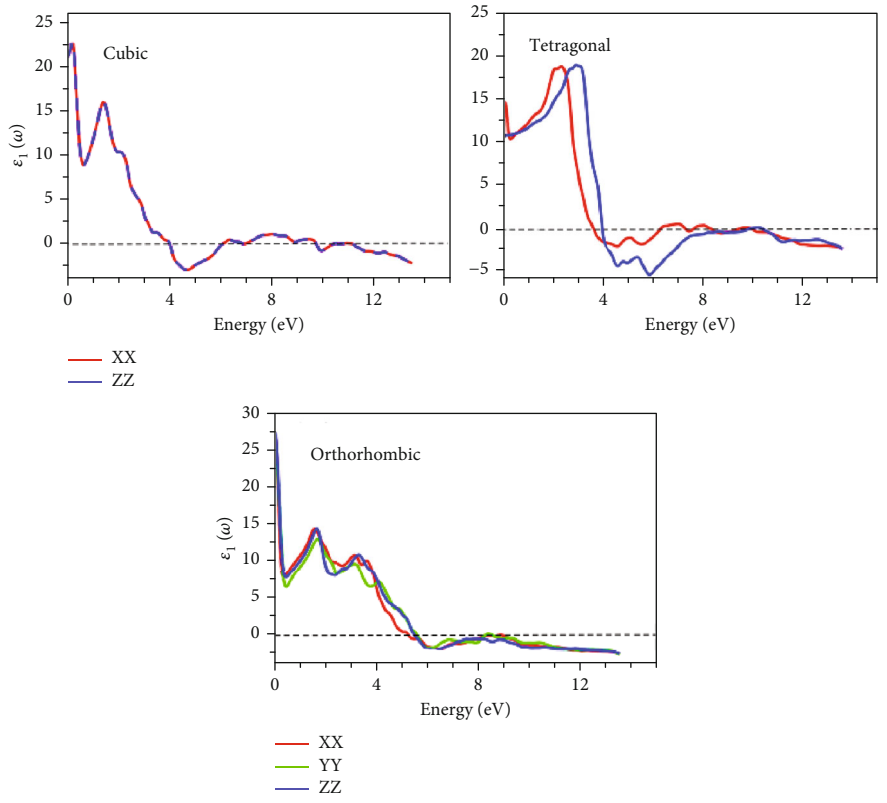

(a)

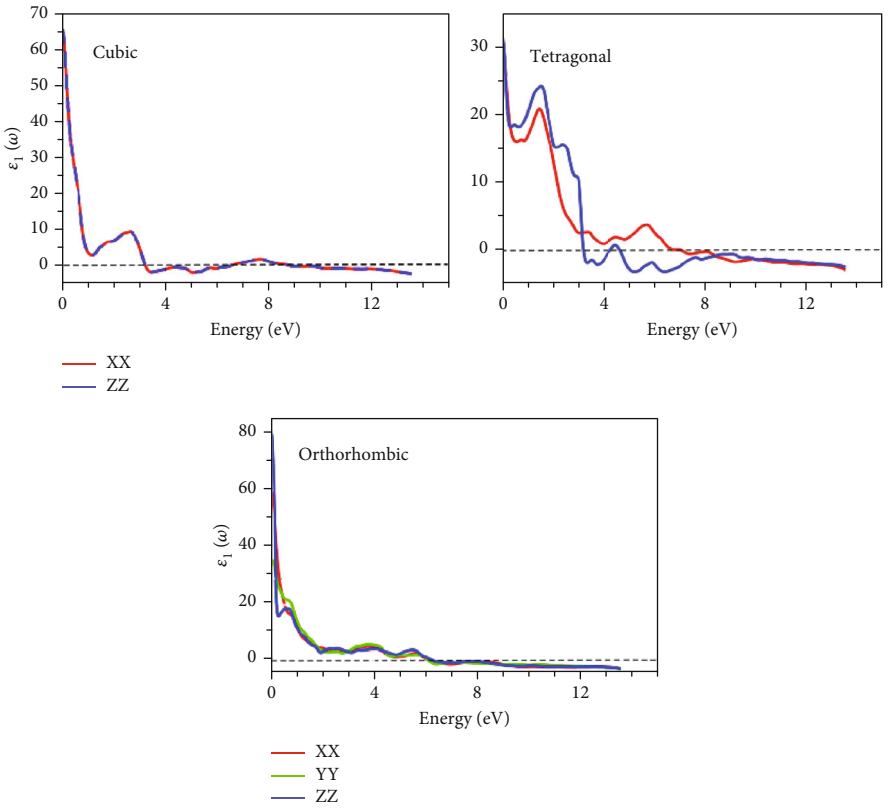

(b)

Figure 12: Continued.

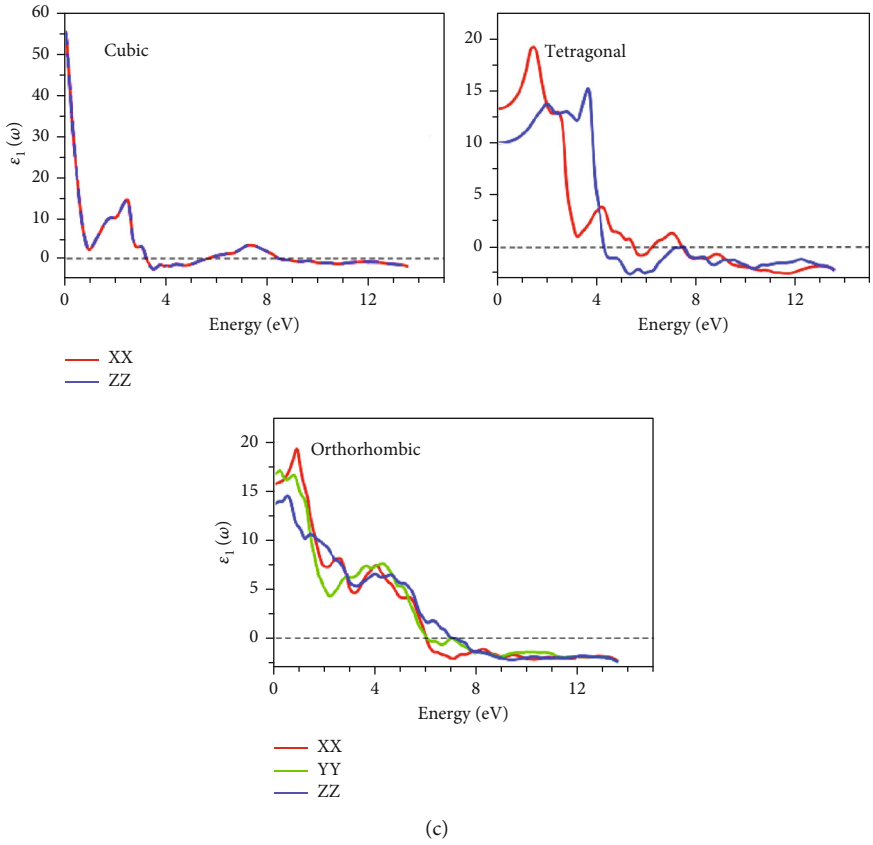

(c)

Figure 12: Real part of dielectric function $\varepsilon_1(\omega)$ spectra of (a) $GeScS_3$, (b) $GeFeS_3$, and (c) $GeZnS_3$.

unoccupied 3d orbitals, the local environment of neighboring atoms, and bond lengths [18]. The examined compounds undergo analysis in three magnetic phases for each space group: ferromagnetic (FM), antiferromagnetic (AFM), and nonmagnetic (NM) as outlined in Tables 2 and 3. As previously mentioned, the most reliably predicted stable phases manifest as ferromagnetic (FM) in 127-P4/mbm for $GeFeS_3$ and nonmagnetic (NM) in 62-Pnma for both $GeScS_3$ and $GeZnS_3$. Notably, the antiferromagnetic (AFM) calculations reveal a complete disappearance of magnetic moment in all compounds. The unfavorable nature of the AFM phase is evident through the formation energy calculations.

In $GeScS_3$, the magnetic properties are absent for both the cubic (221-Pm-3m) and orthorhombic (62-Pnma) phases. However, in the tetragonal phase (127-P4/mbm), magnetism is observable. Note that the magnetism at the interstitial region is higher than that at the atomic sites; this can be attributed to the hybridization of orbitals, especially involving transition metal elements like Sc, which can contribute to magnetic moments. The interaction of the atomic orbitals in the interstitial region may lead to localized magnetic effects.

Conversely, in the $GeFeS_3$ compound, all phases exhibit fairly comparable ferromagnetic behavior, as anticipated, and this behavior is predominantly attributed to iron atom sites. The contributions from Ge and S atoms are minimal and bear negligible values. The contribution of interstitial magnetic moments varies mainly due to fluctuations in the local environment of nearest neighbors. The calculation of the total magnetic moment using mBJ + U at the Fe atom site shows an insignificant variation, as mentioned earlier. It is worth noting that the mapping of magnetic moments can be complex and is often linked to the intricate interactions that transition metal ions exhibit within specific coordination environments involving chalcogenide atoms, such as sulfur in this case [30]. For the $GeZnS_3$ compound, magnetism is absent across all phases and scenarios.

The energy bandgap (Eg) and electronic density of states (DOS) have been thoroughly examined for all structures across various phases. $GeScS_3$ displays metallic behavior in all phases. However, an interesting conduction band intersection with E_F is observed in the spin-up channel of the tetragonal phase, categorizing the compound as a semimetal (Figure 4).

For $GeFeS_3$, the energy band structure unveils a direct $(\Gamma - \Gamma)$ bandgap of 0.235 eV solely in the orthorhombic phase within the spin-up channel (Figure 5(c)); meanwhile, this compound shows metallic behavior in the other space groups like cubic and tetragonal (Figures 5(a) and 5(b)). Conversely, a semiconducting characteristic is demonstrated by an indirect $(X - Z)$ bandgap of 0.827 eV within the tetragonal phase of $GeZnS_3$ (Figure 6(b)) and metallic behavior in the other phases (Figures 6(a) and 6(c)). In order to ensure

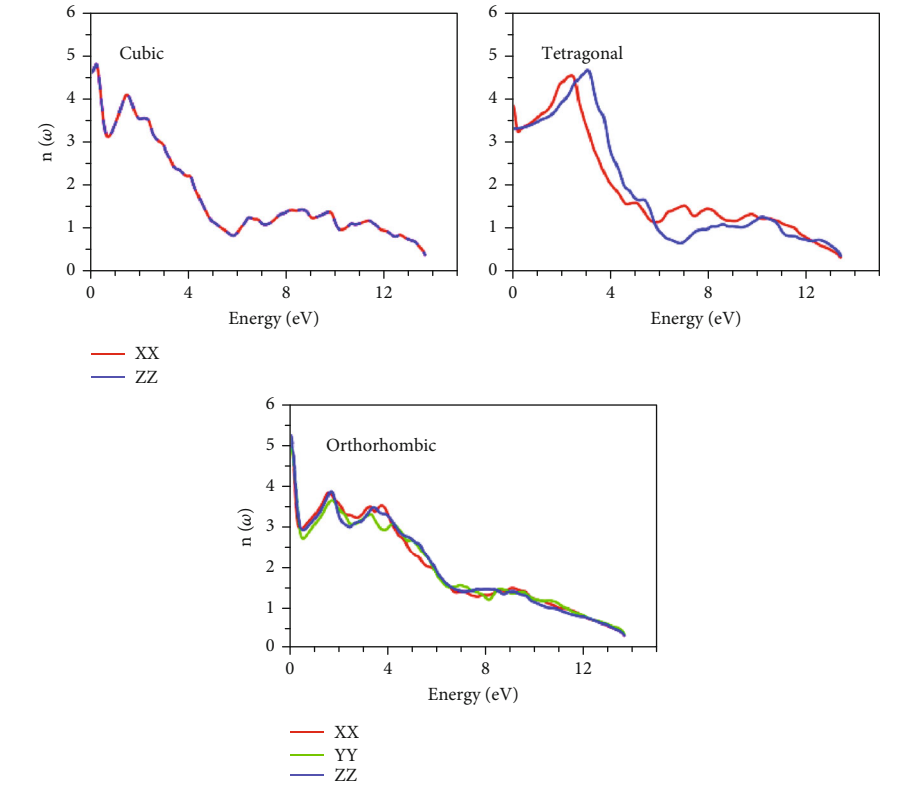

(a)

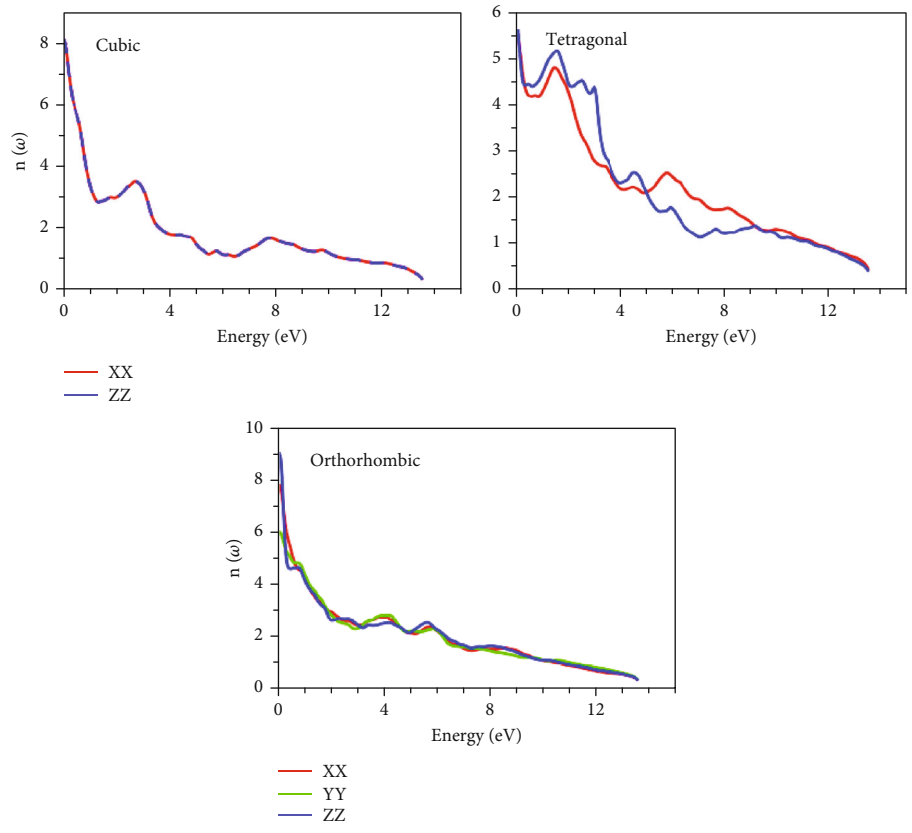

(b)

Figure 13: Continued.

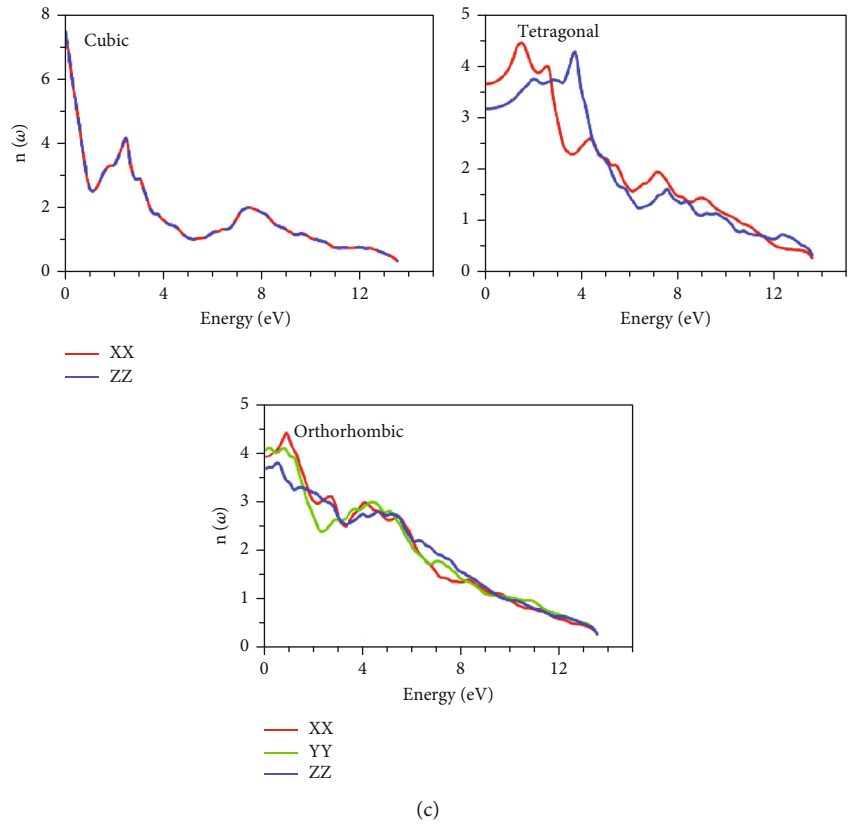

(c)

Figure 13: Refractivity $n(\omega)$ spectra of (a) $GeScS_3$, (b) $GeFeS_3$, and (c) $GeZnS_3$.

the accuracy of band structure calculations, specific paths were adopted, such as (Γ-X-M-Γ-Z-R-A-Z-Γ) and (Γ-X-S-Γ-Y-S) for the tetragonal and orthorhombic phases, respectively, as depicted in Figure 7.

Examination of the total and partial density of states (TDOS and PDOS) reveals that the PDOS concentrated around or near E_F is primarily influenced by the S-p orbital and the TM-d orbital (Figures 8–10). Eventually, $GeFeS_3$ exhibits half-metallic behavior in the orthorhombic phase, displaying 100% spin polarization at E_F, a feature that renders this material suitable for utilization in the spintronic industry. Conversely, the tetragonal phase of $GeZnS_3$ displays semiconducting behavior.

3.2. Optical Properties. The intricate dielectric function, denoted as $\varepsilon(\omega)$ and composed of its two constituent parts $\varepsilon_1(\omega)$ and $\varepsilon_2(\omega)$, is meticulously explored for the studied phases employing the Kramer-Kronig relations [31, 32]. In this context, $\varepsilon_1(\omega)$ and $\varepsilon_2(\omega)$ signify the real and imaginary components of $\varepsilon(\omega)$, respectively. By incorporating the function $\varepsilon(\omega)$ into the Kramer-Kronig relations, it becomes possible to compute a range of spectra including the refractive index $n(\omega)$, reflectivity $R(\omega)$, absorption $I(\omega)$, and energy loss $E_{\text{loss}}(\omega)$, utilizing equations 49 to 54 as referenced in [33].

These spectra are acquired along both the *xx* and *zz* directions for cubic and tetragonal phases, which are notably identical within the cubic phase. However, for the orthorhombic phase, the analysis extends along the *xx*, *yy*, and *z z* directions, showcasing an anisotropic behavior.

The imaginary component of the dielectric function, $\varepsilon_2(\omega)$, is depicted in Figure 11. Evidently, all studied structures across their various phases may exhibit characteristics of a light harvester, as the spectra consistently maintain positive and nonzero values throughout the entire energy range under investigation [34]. As expected, the material's behavior is isotropic in the cubic phase, in contrast to the other phases.

Prominent peaks, identifiable across all phases, are positioned below the 4 eV energy threshold, primarily arising from interband transitions involving the p-orbital of the Ge atom and the d-orbital of the TM (Sc, Fe, Zn) atom. Static $\varepsilon_2(0)$ values are presented in Tables 5–7. The highest $\varepsilon_2(0)$ values are observed in the semiconductor phase, which is orthorhombic for both $GeScS_3$ and $GeFeS_3$ and tetragonal for $GeZnS_3$. This suggests that these structural configurations could potentially serve as efficient light harvesters.

Conversely, the real component, $\varepsilon_1(\omega)$, is illustrated in Figure 12. It is evident that all compounds exhibit metallic behavior as the spectrum transitions into negative values. This phenomenon is observable for $GeScS_3$ across both cubic and tetragonal phases within the energy range of 4 to 8 eV. Similarly, the same metallic trend emerges for

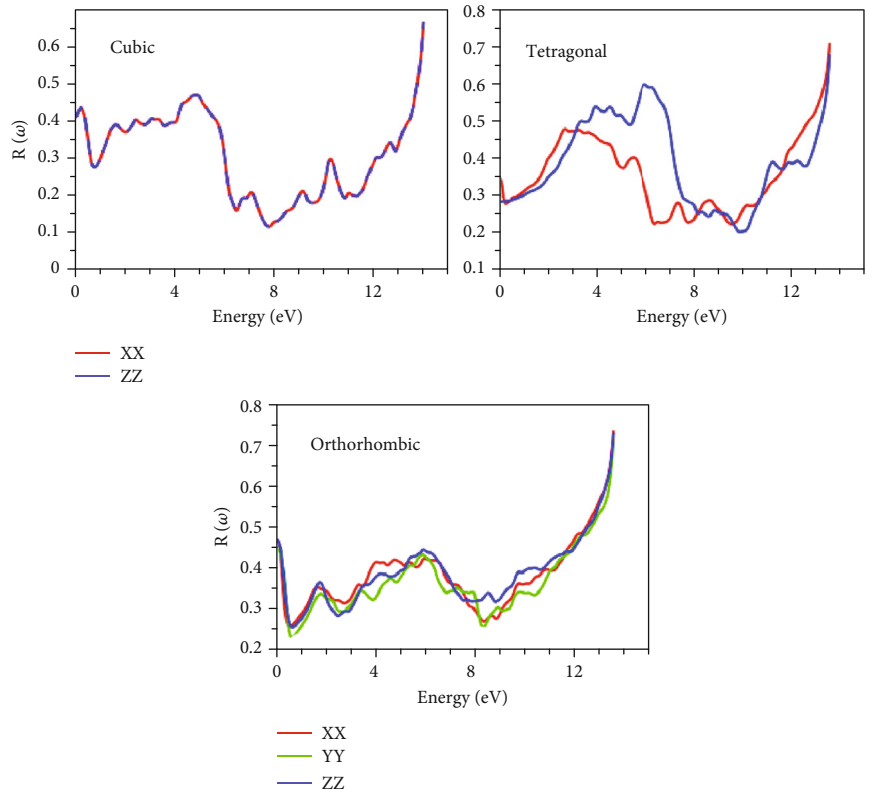

(a)

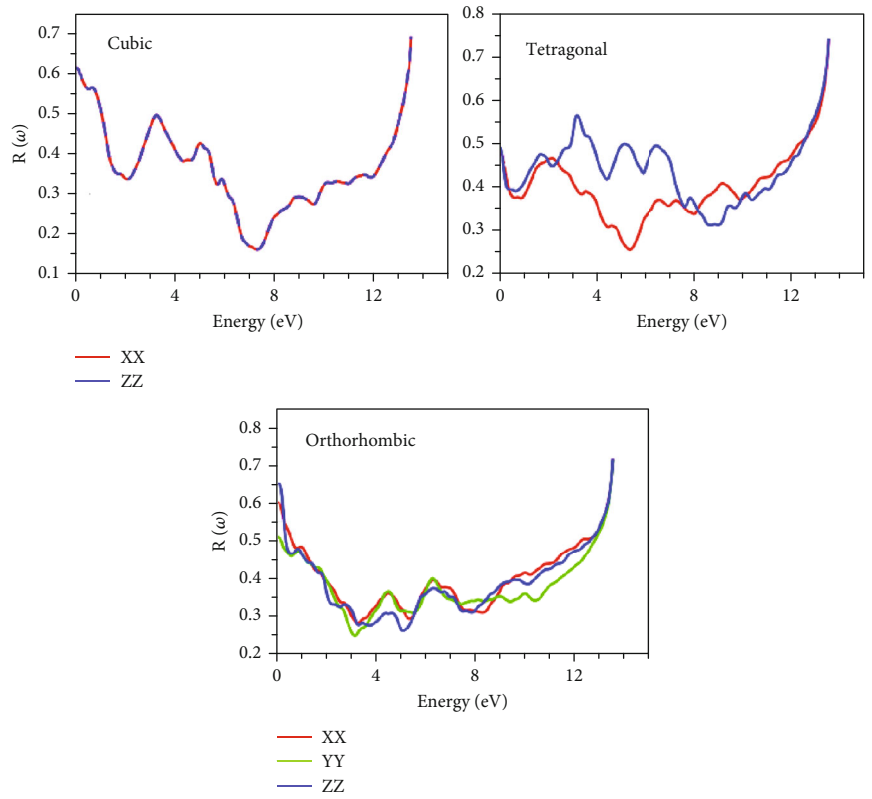

(b)

Figure 14: Continued.

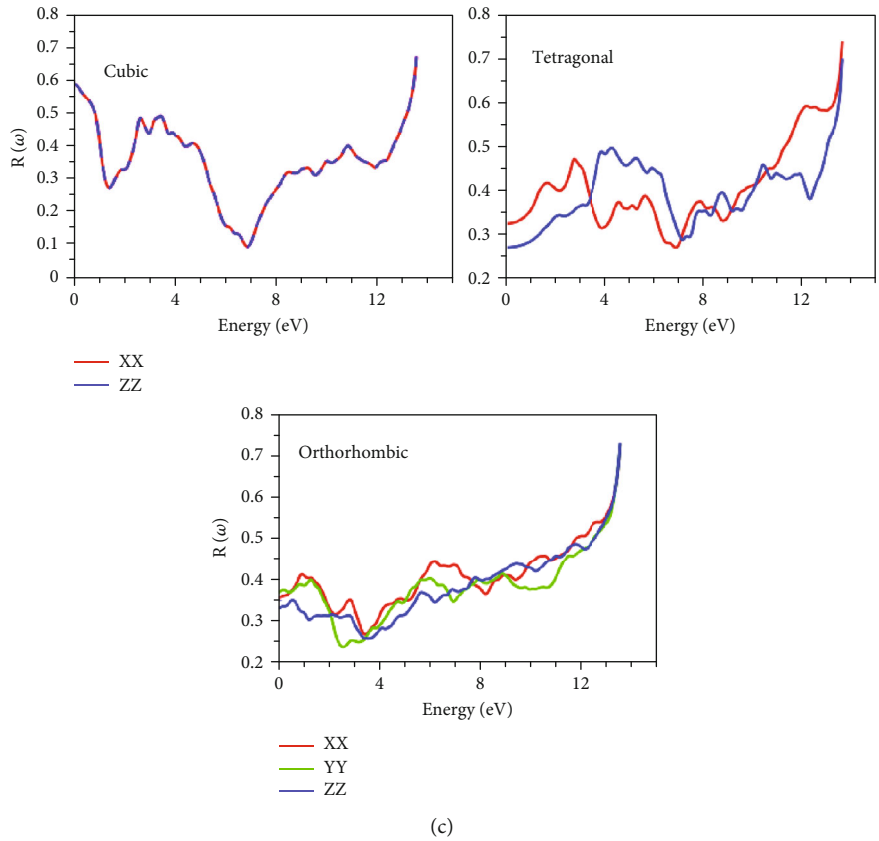

(c)

FIGURE 14: Reflectivity $R(\omega)$ spectra of (a) $GeScS_3$, (b) $GeFeS_3$, and (c) $GeZnS_3$.

the orthorhombic phase beyond 6 eV. In the case of $GeFeS_3$ and $GeZnS_3$, the manifestation of metallicity is observed in energy intervals of 3-6 eV, 3-8 eV, and beyond 8 eV for cubic, tetragonal, and orthorhombic phases, respectively. The static constant values of $\varepsilon_1(0)$ are outlined in Tables 5–7, reflecting distinct values across various directions for each phase. Obviously, the highest value is anticipated in the *zz*-directions of both orthorhombic $GeScS_3$ and $GeFeS_3$. In the case of cubic $GeZnS_3$, the largest $\varepsilon_1(0)$ is found.

The interaction of light with matter is closely linked to the refractive spectrum, which reveals how much light is bent as it traverses a material. It is important to note that the static refractive indices vary across phases, as detailed in Table 5. Notably, the highest static refractive indices are predominantly associated with cubic phases.

Furthermore, prominent peaks are consistently identified in various directions for different phases, predominantly occurring below the 4 eV energy threshold. The refractive spectra reveal resonance in this region, resulting from intraband transitions. As energy levels rise, refractivity decreases, corresponding to the onset of negative values in ε_1. This marks the initiation of metallic behavior, as depicted in Figures 12 and 13.

In Figure 14, the static reflectivity $R(0)$ is computed, revealing values below unity for all phases, as indicated in Table 6. Remarkably, these static values experience a rapid decline within the low energy range, with the lowest points situated in this region. This characteristic renders the material a promising absorbent within this energy range, making it potentially suitable for photovoltaic applications. A significant surge in reflectivity is observed in higher energy regions and beyond, aligning with the manifestation of metallic behavior. This correspondence between the rapid increase in reflectivity and the emergence of negative values in ε_1 reaffirms the presence of metallicity [35].

The absorption process unfolds when the energy of the bandgaps falls below that of the incident photon. As illustrated in Figure 15, the spectral components of the absorption coefficient $I(\omega)$ are showcased for each material. Characterized by three components (x, y, and z), the overall profiles of these spectra exhibit a consistent pattern across our various compounds. Upon closer inspection of the curve features, a noticeable trend emerges—the initial stages of absorption witness a surge in spectra energies aligned with the optical gap in the orthorhombic configurations for $GeScS_3$ and $GeFeS_3$, as well as the tetragonal structure for $GeZnS_3$. Interestingly, the absorption spectra extend into both the visible and ultraviolet spectra. This behavior suggests the potential suitability of these materials, positioning them as promising candidates for applications such as the window layer in solar cells and flat-panel displays.

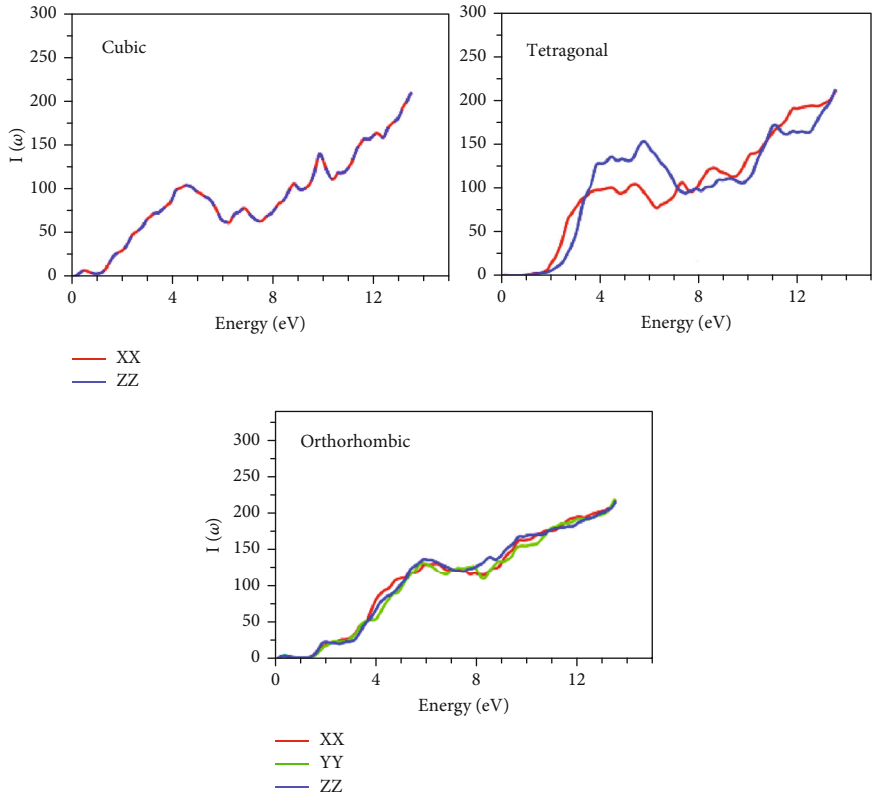

(a)

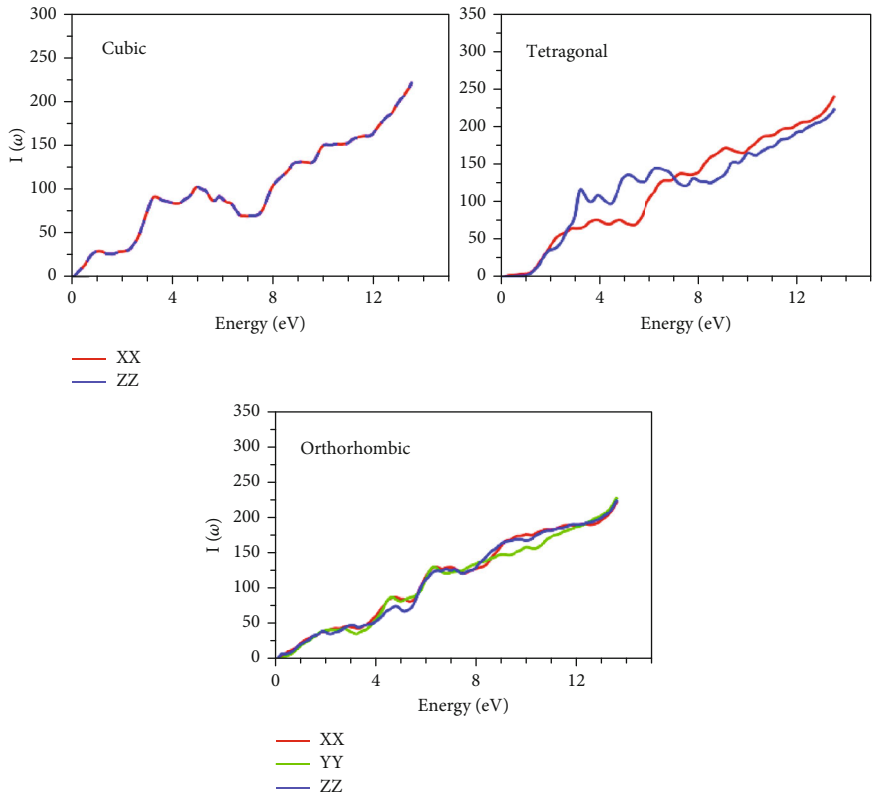

(b)

Figure 15: Continued.

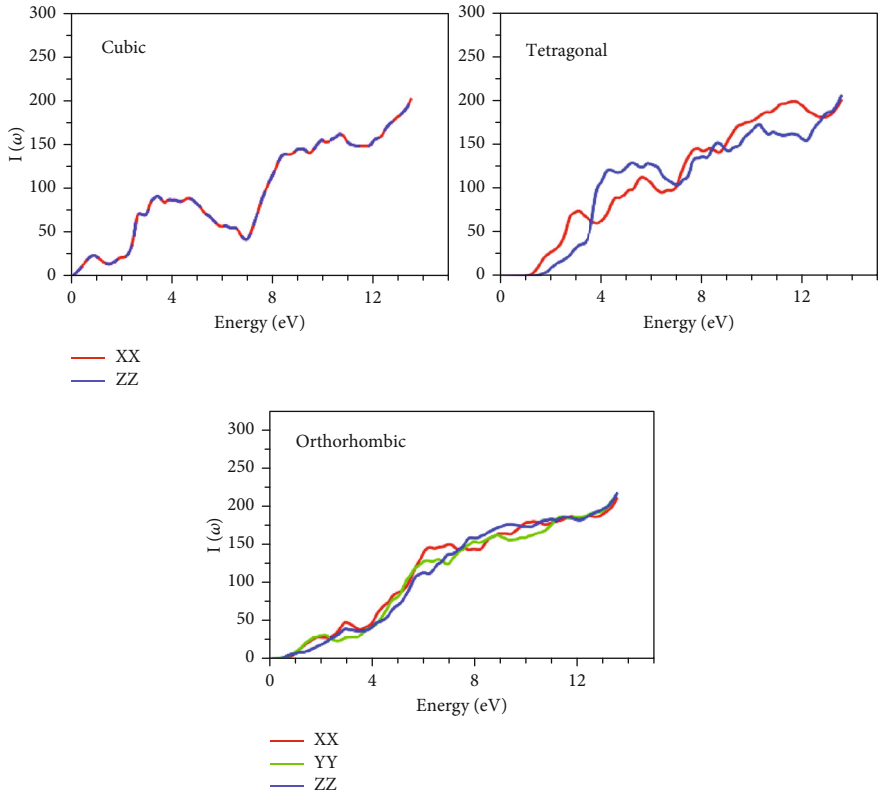

(c)

FIGURE 15: Absorption $I(\omega)$ spectra of (a) $GeScS_3$, (b) $GeFeS_3$, and (c) $GeZnS_3$.

The quantification of energy absorbed through the material is effectively represented by the E_{loss} function, as depicted in Figure 16. Conspicuously, the minimum E_{loss} values are consistently situated below 4 eV for all phases, aligning with the anticipated maxima of the refractive function $n(\omega)$. As energy levels surpass 4 eV, E_{loss} experiences an increment, consistent with the concurrent rise in refractivity within that energy range.

4. Conclusion

In conclusion, this comprehensive study has delved into the structural, electronic, magnetic, and optical properties of sulfide perovskite $GeTMS_3$(TM=Sc, Fe, Zn) across its cubic, tetragonal, and orthorhombic phases. Through extensive calculations employing DFT-FP-LAPW methods and GGA-mBJ potentials, we have gained valuable insights into the behavior and characteristics of these materials.

The investigation has revealed intriguing findings regarding the stability and behavior of various phases. The energetic calculations, cohesive energy values, and Gibbs free energy analysis have provided a comprehensive understanding of the most stable phases for different compositions. The examination of magnetic behavior has elucidated the influence of transition metal atoms, with $GeZnS_3$ and $GeScS_3$ exhibiting nonmagnetic behavior, while $GeFeS_3$ showcases ferromagnetic properties across all phases, particularly at iron atom sites.

The electronic properties, including the energy bandgaps and density of states, have highlighted the semiconducting and metallic behaviors exhibited by different phases. Particularly notable is the half-metallic behavior observed in the orthorhombic phase of $GeFeS_3$, making it a promising candidate for spintronic applications.

The investigation of optical properties showcased the potential of these materials as light harvesters, with positive and nonzero $\varepsilon_2(\omega)$ spectra indicative of their suitability for energy conversion applications. Refractive indices varied with phases, with cubic phases often exhibiting the highest static refractive indices. The presence of metallic behavior was consistent with the negative values of $\varepsilon_1(\omega)$, while absorbent characteristics in the low energy range marked these materials as potential candidates for photovoltaic applications.

In summary, our study sheds light on the multifaceted nature of sulfide perovskite $GeTMS_3$, offering valuable insights into their properties and potential applications in various technological fields. Our findings place a strong emphasis on the contemporary applications of sulfide perovskites, shedding light on their practical relevance in current technological landscapes. By closely examining their performance in diverse applications such as photovoltaics and spintronics, we aim to not only enrich our understanding

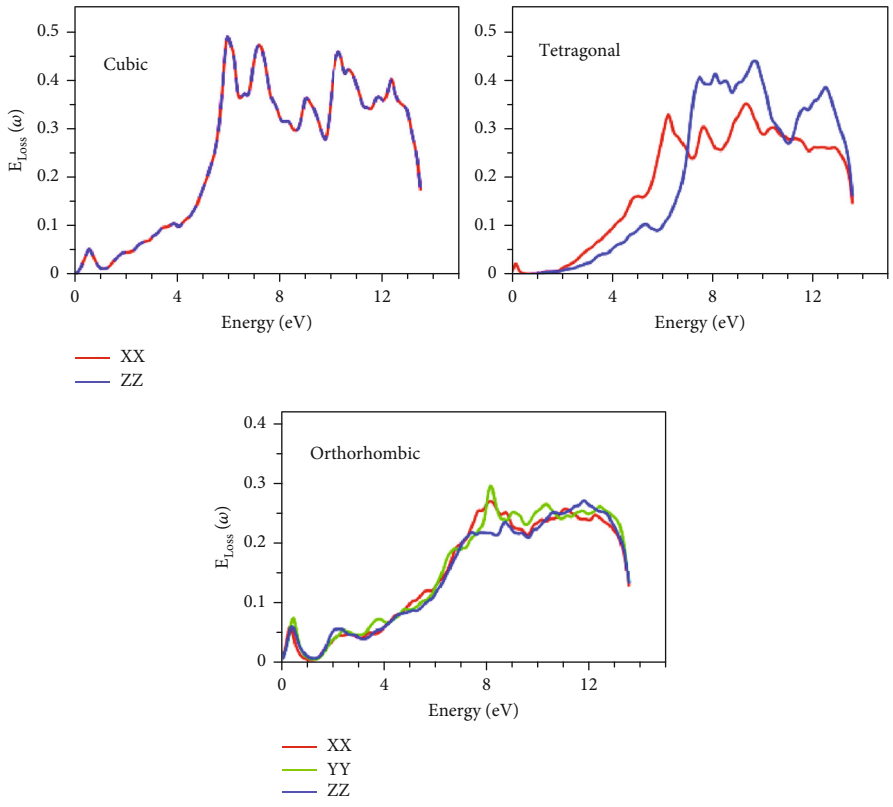

(a)

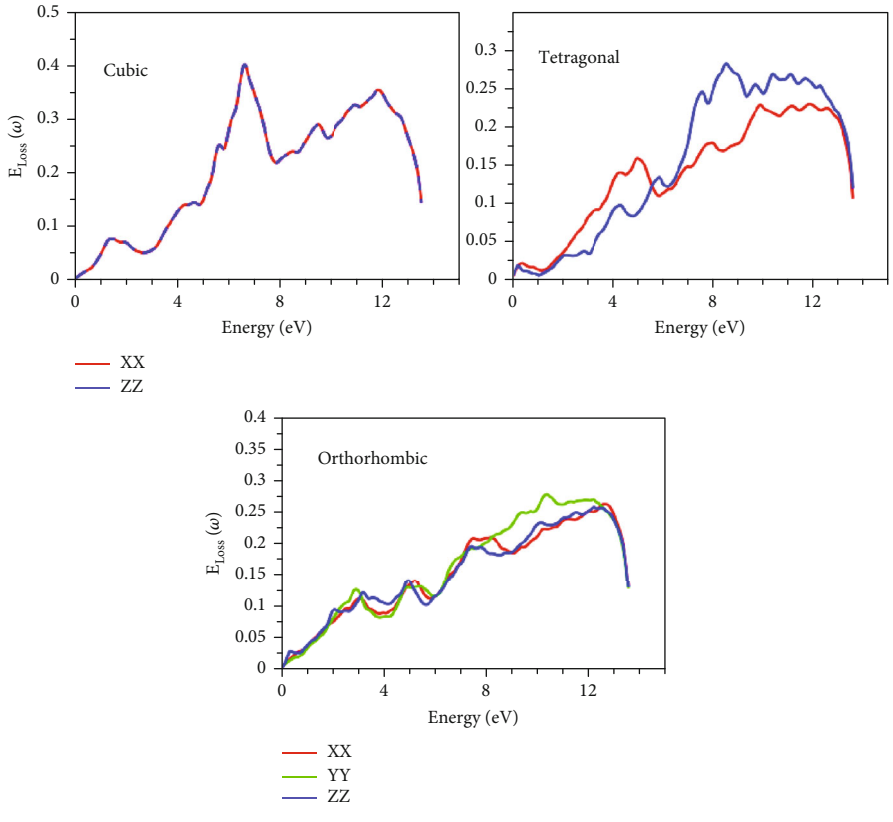

(b)

Figure 16: Continued.

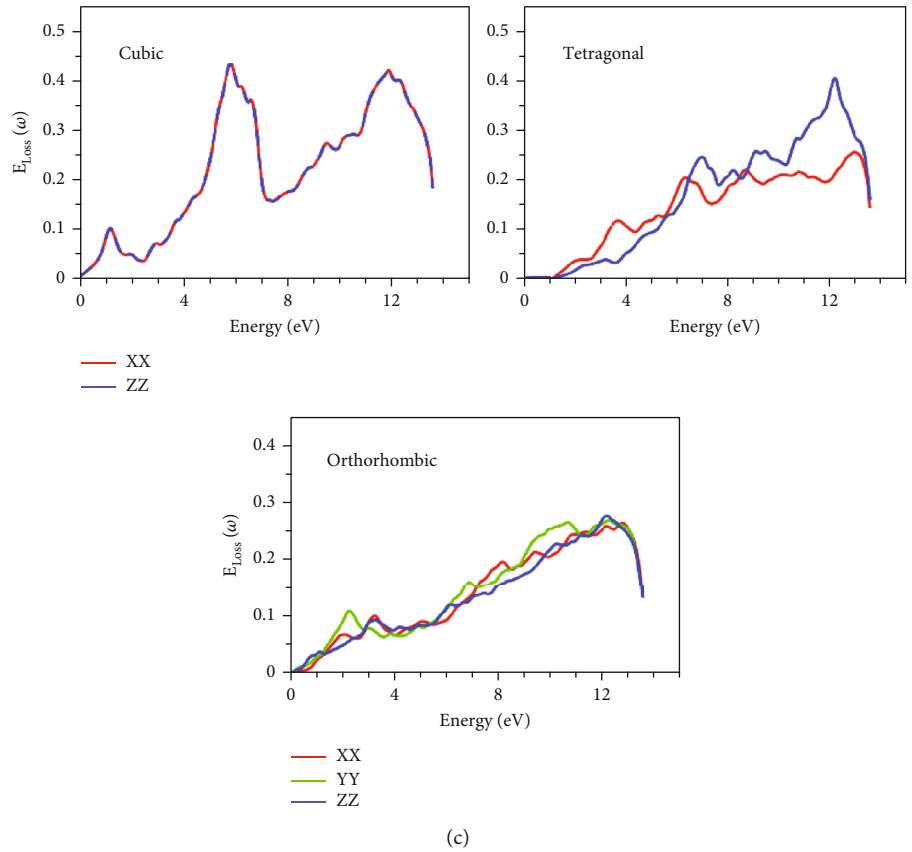

(c)

FIGURE 16: Energy loss function $E_{loss}(\omega)$ of (a) $GeScS_3$, (b) $GeFeS_3$, and (c) $GeZnS_3$.

of these materials in their present context but also pave the way for future advancements. Our exploration of current applications serves as a foundation for unraveling the untapped potential of sulfide perovskites, offering a comprehensive perspective that extends beyond the immediate present into the promising future of materials science and technology.

Data Availability

The data supporting the conclusions of this research are accessible from the corresponding author upon making a reasonable request.

Disclosure

We, the authors of this manuscript, hereby affirm the originality of our submitted work. The raw data for this study were produced at the University of Jordan.

Conflicts of Interest

The authors declare that they have no conflicts of interest.

References

[1] M. Imada, A. Fujimori, and Y. Tokura, "Metal-insulator transitions," *Reviews of Modern Physics*, vol. 70, no. 4, pp. 1039–1263, 1998.

[2] A. S. Bhalla, R. Guo, and R. Roy, "The perovskite structure – a review of its role in ceramic science and technology," *Materials Research Innovations*, vol. 4, pp. 3–26, 2000.

[3] H. S. Kim, C. R. Lee, J. H. Im et al., "Lead iodide perovskite sensitized all-solid-state submicron thin film mesoscopic solar cell with efficiency exceeding 9%," *Scientific Reports*, vol. 2, no. 1, p. 591, 2012.

[4] T. Brenner, D. Egger, L. Kronik, G. Hodes, and D. Cahen, "Hybrid organic—inorganic perovskites: low-cost semiconductors with intriguing charge-transport properties," *Nature Reviews Materials*, vol. 1, no. 1, article 15007, 2016.

[5] M. Zhang, M. Lyu, J. Yun et al., "Low-temperature processed solar cells with formamidinium tin halide perovskite/fullerene heterojunctions," *Chemistry - A European Journal*, vol. 9, pp. 570–1577, 2016.

[6] K. Kuhar, A. Crovetto, M. Pandey et al., "Sulfide perovskites for solar energy conversion applications: computational screening and synthesis of the selected compound $LaYS_3$," *Energy & Environmental Science*, vol. 10, no. 12, pp. 2579–2593, 2017.

[7] A. Crovetto, R. Nielsen, M. Pandey et al., "Shining light on sulfide perovskites: LaYS3material properties and solar cells," *Chemistry of Materials*, vol. 31, no. 9, pp. 3359–3369, 2019.

[8] X. Wei, H. Hui, C. Zhao et al., "Realization of $BaZrS_3$ chalcogenide perovskite thin films for optoelectronics," *Nano Energy*, vol. 68, article 104317, 2020.

[9] N. T. Mahmoud, A. A. Mousa, and J. M. Khalifeh, "First principles investigation of thermoelectric and mechanical properties of VScO3 semiconductor perovskite for sustainable and

renewable energy," *Results in Physics*, vol. 18, article 103331, 2020.

[10] A.-Q. Samah, D. P. Rai, T. Alshahrani et al., "Structural, elastic, thermodynamic, electronic, optical and thermoelectric properties of MgLu2X4 (X= S, Se) spinel compounds from ab-initio calculations," *Materials Science in Semiconductor Processing*, vol. 128, article 105766, 2021.

[11] A. Swarnkar, W. J. Mir, R. Chakraborty, M. Jagadeeswararao, T. Sheikh, and A. Nag, "Are chalcogenide perovskites an emerging class of semiconductors for optoelectronic properties and solar cell?," *Chemistry of Materials*, vol. 31, no. 3, pp. 565–575, 2019.

[12] S. Niu, H. Huyan, L. Yang et al., "Bandgap control via structural and chemical tuning of transition metal perovskite chalcogenides," *Advanced Materials*, vol. 29, no. 9, article 1604733, 2017.

[13] P. Basera and S. Bhattacharya, "Chalcogenide perovskites (ABS_3; A = Ba, Ca, Sr; B = Hf, Sn): an emerging class of semiconductors for optoelectronics," *Journal of Physical Chemistry Letters*, vol. 13, no. 28, pp. 6439–6446, 2022.

[14] Y.-Y. Sun, M. L. Agiorgousis, P. Zhang, and S. Zhang, "Chalcogenide perovskites for photovoltaics," *Nano Letters*, vol. 15, no. 1, pp. 581–585, 2015.

[15] G. Bennett, H. Takenaka, and A. M. Rappe, "Effect of substituting of S for O: the sulfide perovskite $BaZrS_3$ investigated with density functional theory," *Physical Review B*, vol. 79, no. 23, article 235115, 2009.

[16] S. Perera, H. Hui, C. Zhao et al., "Chalcogenide perovskites – an emerging class of ionic semiconductors," *Nano Energy*, vol. 22, pp. 129–135, 2016.

[17] N. T. Mahmoud, B. Malaji, A. A. Mousa, and J. M. Khalifeh, "Effect of the"3-d" band filling on the structural, electronic, magnetic and optical properties of $TMScO_3$ perovskite," *Chinese Journal of Physics*, vol. 65, pp. 500–512, 2020.

[18] N. T. Mahmoud, A. A. Mousa, and J. M. Khalifeh, "Effects of rare earth element Eu on structural, electronic, magnetic, and optical properties of fluoroperovskite compounds $SrLiF_3$: first principles calculations," *Physica B: Condensed Matter*, vol. 564, pp. 37–44, 2019.

[19] N. T. Mahmoud, J. M. Khalifeh, and A. A. Mousa, "Ab-initio investigations of the structural, electronic, magnetic and optical properties of $Ca_{1-x}Eu_xLiF_3$ fluoroperovskite," *Computational Condensed Matter*, vol. 21, article e00432, 2019.

[20] W. Kohn and L. J. Sham, "Self-consistent equations including exchange and correlation effects," *Physical Review*, vol. 140, no. 4A, pp. A1133–A1138, 1965.

[21] P. Blaha, P. Blaha, K. Schwarz et al., *WIEN2k: an APW+lo program for calculating the properties of solids*, Technical Universita¨t WIEN, Austria, 2001.

[22] J. P. Perdew, K. Burke, and M. Ernzerhof, "Generalized gradient approximation made simple," *Physical Review Letters*, vol. 77, no. 18, pp. 3865–3868, 1996.

[23] F. Tran and P. Blaha, "Accurate band gaps of semiconductors and insulators with a semilocal exchange-correlation potential," *Physical Review Letters*, vol. 102, no. 22, article 226401, 2009.

[24] F. D. Murnaghan, "The compressibility of media under extreme pressures," *Proceedings of the National Academy of Sciences*, vol. 30, no. 9, pp. 244–247, 1944.

[25] P. E. Blöchl, O. Jepsen, and O. K. Andersen, "Improved tetrahedron method for Brillouin-zone integrations," *Physical Review B*, vol. 49, article 16223, 1994.

[26] S. A. Khandy, I. Islam, D. C. Gupta, R. Khenata, and A. Laref, "Lattice dynamics, mechanical stability and electronic structure of Fe-based Heusler semiconductors," *Scientific Reports*, vol. 9, no. 1, p. 1475, 2019.

[27] M. Cococcioni and S. de Gironcoli, "Linear response approach to the calculation of the effective interaction parameters in theLDA+Umethod," *Physical Review B*, vol. 71, no. 3, article 035105, 2005.

[28] J. Williard Gibbs, *Elementary Principles in Statistical Mechanics*, Ox Bow Press, 1902.

[29] P. Lemmens and P. Millet, "Spin—orbit—topology, a triptych," in *Quantum Magnetism*, pp. 433–477, Springer, Heidelberg, 2004.

[30] M. Fox, *Optical Properties of Solids*, Oxford University Press, New York, 2001.

[31] M. Dressel and G. Gruner, *Electrodynamics of Solids: Optical Properties of Electrons in Matter*, Cambridge University Press, UK, 2010.

[32] N. T. Mahmoud, A. A. Mousa, H. K. Juwhari, J. M. Khalifeh, and M. S. Abu-Jafar, "Optical dispersion functions of $Co_{2-x}Eu_xVSn$ using *ab-initio* calculations," *International Journal of Modern Physics B*, vol. 29, no. 28, article 1550195, 2015.

[33] M. S. Abu-Jafar, V. Leonhardi, R. Jaradat et al., "Structural, electronic, mechanical, and dynamical properties of scandium carbide," *Results in Physics*, vol. 21, article 103804, 2021.

[34] M. Petrović, V. Chellappan, and S. Ramakrishna, "Perovskites: solar cells & engineering applications – materials and device developments," *Solar Energy*, vol. 122, pp. 678–699, 2015.

[35] N. T. Mahmoud, A. A. Musa, and A. A. Shaheen, "Effect of doping titanium ions on semi-conducting behavior, photovoltaic, and thermoelectric perovskite-type oxides $VSc_{1-x}Ti_xO_3$: ab-inito study," *International Journal of Energy Research*, vol. 46, no. 9, pp. 12184–12206, 2022.